Advanced Fiber Materials
https://doi.org/10.1007/s42765-025-00658-y

REVIEW

Advances in Melt-Electrowriting of Fibrous Bioscaffolds: A High-Resolution Manufacturing Strategy for Tissue Regeneration

Jinqiao Jia[1] · Qi Lei[2,3] · Zhengjiang Liu[2] · Xiumei Zhang[2] · Xiaomin Guan[2] · Zhicheng Bai[1] · Shilei Zhu[1] · Ya Nan Ye[1] · Jinke Chang[4,5] · Di Huang[2,3]

Received: 6 September 2025 / Accepted: 4 December 2025

Abstract
Melt-electrowriting (MEW) is a high-resolution additive manufacturing technique that has demonstrated significant progress in recent years. Owing to its precise control over fiber deposition, MEW is especially suitable for fabricating fine structures that mimic the natural extracellular matrix (ECM), thereby presenting considerable promise for applications in tissue engineering and regeneration. This review systematically examines the fundamental design principles and recent progress in MEW-based strategies for different tissue engineering and regeneration fields. Initially, the components of the MEW system, the underlying printing mechanisms, and the role of key process parameters are introduced, thereby providing a comprehensive framework for the rational design of scaffolds that replicate both the structural and functional characteristics of native ECM. Subsequently, the selection and performance of commonly employed biomaterials are discussed, with an emphasis on the versatility for diverse tissue engineering applications. The integration of MEW with bioactive materials is further highlighted as an effective approach to enhance the biological functionality of printed constructs and extend their therapeutic potential. Finally, current challenges and future perspectives are outlined, aiming to guide ongoing research and facilitate the clinical translation of MEW-based biofabrication technologies.

Keywords Melt-electrowriting · Fibrous scaffolds · Micro/nanoscale architectures · Bioactive materials · Tissue engineering

1 Introduction

Constructing functional micro/nanoscale structures to mimic the extracellular matrix (ECM) is important for tissue regeneration in vitro and in vivo [1, 2]. As a complex architecture, the ECM exerts pivotal influences on various biological functions: (i) the ECM provides attachment cues for cells and organizes the individual cells into three-dimensional (3D) tissues [3]. (ii) ECM plays a dominant role in supporting the transport of nutrients to promote metabolic processes [4]. (iii) As an intricate network composed of multiple biomacromolecules, ECM can deliver topographical

✉ Qi Lei
leiqi@tyut.edu.cn

✉ Ya Nan Ye
yeyanan@tyut.edu.cn

✉ Jinke Chang
jinke.chang@ucl.ac.uk

✉ Di Huang
huangjw2067@163.com

[1] College of Materials Science & Engineering, Taiyuan University of Technology, Taiyuan 030024, People's Republic of China

[2] Department of Biomedical Engineering, Research Center for Nano-Biomaterials & Regenerative Medicine, Shanxi Key Laboratory of Functional Proteins, College of Artificial Intelligence, Taiyuan University of Technology, Taiyuan 030024, People's Republic of China

[3] Institute of Biomedical Engineering, Shanxi Key Laboratory of Materials Strength & Structural Impact, Taiyuan University of Technology, Taiyuan 030024, People's Republic of China

[4] Division of Surgery and Interventiosnal Science, University College London, London NW3 2PF, UK

[5] Department of Engineering Science, University of Oxford, Oxford OX1 3PJ, UK

Published online: 03 January 2026

and biological signals, such as integrins, proteoglycans, and growth factors [5]. Therefore, an ideal artificial micro/nanoscale structure should possess a 3D architecture, nutrient channels, and topographical cues. In addition, therapeutic applications require appropriate structural dimensions and suitable mechanical properties for suturing [6, 7].

To accurately replicate the functional native ECM structure, researchers have extensively endeavored using various methods [8]. For instance, electrospinning is a typical technique employed to fabricate sub-microscale or nanoscale fibrous architectures, which can provide topographical cues for cells [9–11]. Furthermore, functional nanomaterials and bioactive factors are added to the electrospun fibrous films to regulate cellular behaviors, such as proliferation and differentiation [12, 13]. However, the random fiber orientation inherent to electrospinning limits its ability to replicate the organized 3D architecture of native ECM.

Additive manufacturing is a highly controllable manufacturing approach to fabricate structures with precise geometries, which has found widespread application [14, 15]. For example, two-photon polymerization and fused deposition modeling (FDM) printing are widely used to fabricate 3D architectures for tissue engineering applications. Two-photon polymerization enables to produce 3D structures with the smallest feature size down to nanometer scale, which provides an accurate tool to regulate cellular behaviors [16]. However, this method commonly requires expensive optical systems and specific photosensitive polymers which limits its biological applications. Moreover, FDM technique can produce sturdy and durable parts, thus is widely used in bone tissue substitutes. Teixeira et al. constructed a 3D-printed poly(lactic acid) (PLA) scaffold with poly-dopamine and collagen I coating by FDM, which exhibited an enhanced osteoinductivity. However, the FDM method unable to construct scaffolds with high-resolution and small pore diameters, which is not beneficial to cell-scaffold interaction [17].

Recently, electrohydrodynamic (EHD) printing has emerged as a high-resolution 3D printing technique to fabricate micro/nanoscale fibrous structures mimicking the ECM [18–20]. This printing technique precisely constructs micro/nanoscale fibrous scaffolds through fiber deposition, which combines elements of electrohydrodynamical fiber attraction and melt extrusion [21, 22]. EHD printing enables the creation of a biomimetic microenvironment with 3D structures to support cell growth and migration. The 3D porous structure has the ability to facilitate nutrient transfer, thereby regulating cell growth, proliferation, and activity [23]. As a specialized branch of EHD printing, Melt-electrowriting (MEW) can construct artificial tissue analogs using melt-based polymers as printing materials [24, 25]. Compared to solution-based EHD printing, MEW exhibits advantages, such as solvent-free processing and enhanced process stability. These benefits not only mitigate the risk of toxic residues but also improve controllability, which is facilitated by a lower surface charge density [26]. Moreover, surface modification of specific materials and the incorporation of related growth factors broaden the application scope of MEW in engineering various tissues. Hence, this unique printing method holds great promise for the precise production of micro/nanoscale fibrous scaffolds for tissue engineering.

This article reviews the latest progress in MEW, focusing on the fabrication of artificial tissue analogs as implantable materials for treating injuries and diseases. We summarize the principles, process parameters, and common biomaterials used in the MEW process. Furthermore, we highlight typical applications of MEW fibrous scaffolds in different tissues, involving cardiac tissues, bones, cartilages, vascular, ligaments and tendons, periodontal tissues, and nerves (Fig. 1). Finally, this review provides new insights into the design concept of the tissue engineering scaffolds with an emphasis on the latest designs and innovations of MEW scaffolds, especially in terms of their 3D structure, mechanical properties, and incorporation of bioactive materials. Finally, the main challenges and future perspectives are comprehensively summarized and discussed to inform future research directions.

2 Fundamentals and Mechanism of Melt-Electrowriting

A typical MEW system comprises a glass syringe equipped with a heating sleeve, a high-voltage source, a computer-aided translating system, and a collector (Fig. 2a) [27, 28]. During the MEW process, materials are melted within the syringe and then extruded through a metal nozzle under pressure (air pressure or mechanical extrusion). Meanwhile, a high voltage was applied to the nozzle, and the charged pendant droplet deformed to a conical shape (*Taylor cone*) (Fig. 2b). As the voltage intensifies, the cone further sharpens to achieve equilibrium between the electric field force and surface tension. When the charges overcome the surface tension, a charged jet is ejected toward the collector [29]. This process arises from the equilibrium of forces between gravity, surface tension, internal hydrostatic pressure, external gas pressure, and the electric force [21]. When the printing speed exceeds the translation speed, a phenomenon known as "jet lag" occurs, where the contact point of the polymer jet lags behind the nozzle [30]. Moreover, as the material droplets are deposited, charges are transferred to the conductive substrate and grounded [31]. With the assistance of the computer-aided translating system, the microscale fibers are deposited onto the collector substrate according to a specific path, thereby constructing the fibrous scaffolds. Furthermore, MEW integrates structural design with customized programs, making it possible to develop optimized biomimetic structures [32].

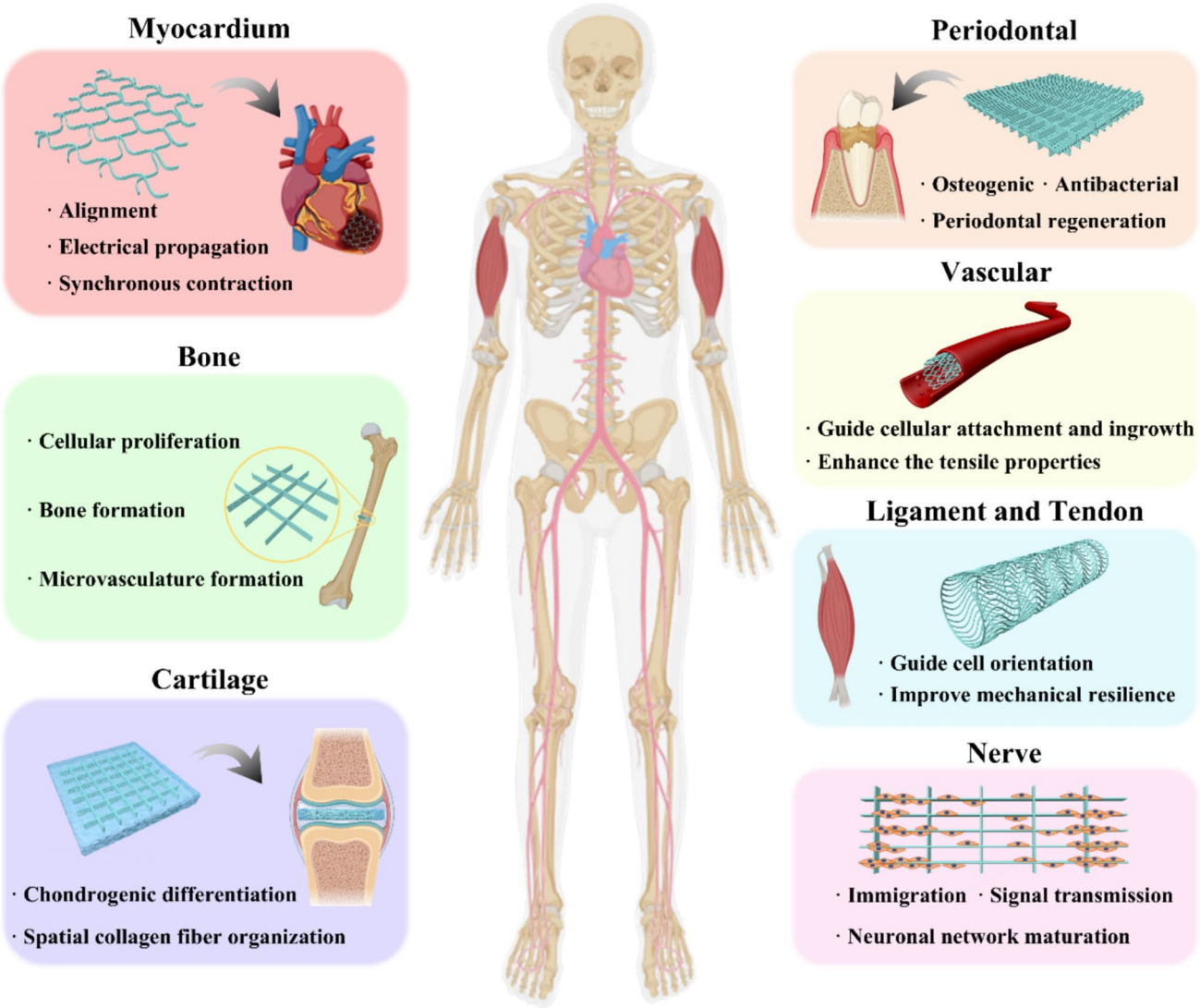

Fig. 1 Advances in the application of MEW in tissue engineering and regeneration. The schematic indicates the advantages of MEW on constructing functional scaffolds and replicating the intricate structure of ECM

To attain a consistent fiber diameter and a stable scaffold structure, the optimization of process parameters has been thoroughly examined. Significant efforts have been directed toward refining key parameters, including the applied voltage, feed rate, nozzle-to-collector distance, collector velocity, and the type of collector [33–37]. Through optimization of the parameters, MEW can fabricate a full spectrum of various fibers with discrete diameters using a single nozzle [27, 38]. The voltage applied between the nozzle and collector directly influences the electrostatic forces and the maintenance of the *Taylor cone*, ultimately impacting printing accuracy. Therefore, during the layer-by-layer stacking process, maintaining a constant electrostatic force is crucial to minimize [39]. The feed rate (controlled by pressure) determines the diameter of the fiber, and the diameter of the fiber increases as the feed rate increases. However, the feed rate must be kept within an optimal range to prevent the material from extrusion difficulties and jet instability. The distance between the nozzle and the collector also plays a pivotal role in influencing the electric field strength, which in turn affects the formation of the *Taylor cone* and the jet. Collector velocity significantly impacts both the fiber diameter and the jet morphology. As the velocity increases, the jet exhibits three distinct morphologies. The minimum velocity that allows for the printing of linear fibers is termed as the critical translation speed (CTS) [40]. At this speed, the jet is perpendicular to the collector substrate and the collected fibers are straight. Below the CTS, the jet vibrates and causes the collected fibers to be coiled or sinusoidal (Fig. 2c) [18, 41, 42]. Above the CTS, the angle between the

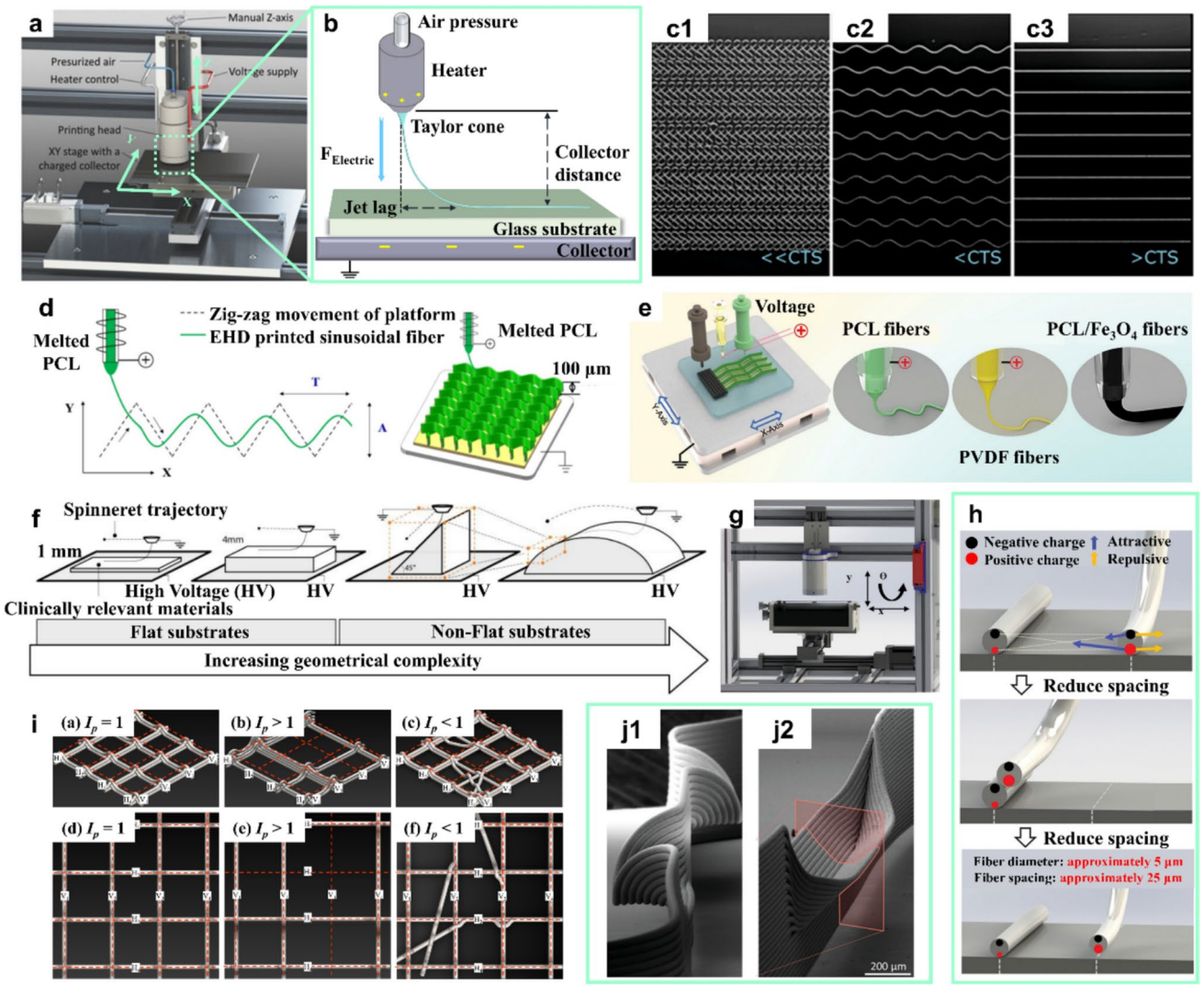

Fig. 2 Principle and strategies for realizing the intricate structures of MEW technique. **a** Components of a MEW system; Reproduced with permission from Ref. [27], Copyright 2018, Wiley–VCH. **b** Schematic of the MEW working principle during the printing process. **c** Coiling (**c1**), sinusoidal (**c2**), and straight (**c3**) fibers printed at below and above CTS speeds; Reproduced with permission from Ref. [18], Copyright 2018, Wiley–VCH. **d** Principle of EHD printing of sinusoidal PCL fibers; Reproduced with permission from Ref. [43], Copyright 2024, American Chemical Society. **e** Schematics of multi-material printing of piezoelectric cardiac microarchitectures combining melt-based, solution-based EHD printing and extrusion printing processes; Reproduced with permission from Ref. [44], Copyright 2024, Wiley–VCH. **f** Schematic of different collector substrates ranging from flat to wedge and curved dome-shaped structures; Reproduced with permission from Ref. [45], Copyright 2020, Elsevier. **g** Mandrel collector as printing substrate; Reproduced with permission from Ref. [47], Copyright 2022, Wiley–VCH. **h** Illustration of fiber deviation phenomena during printing process; reproduced with permission from Ref. [51], Copyright 2022, Elsevier. **i** Schematic of reducing fiber diameter to realize smaller fiber spacing; Reproduced with permission from Ref. [52], Copyright 2023, Wiley–VCH. **j** Overhang (**j1**) structure, and branches (**j2**) of fiber wall into two overhangs; Reproduced with permission from Ref. [53], Copyright 2020, Wiley–VCH

fiber and the collector substrate decreases, and the degree of jet lag increases, resulting in smaller fiber diameters [21]. In another study, sinusoidal fibrous scaffolds were fabricated based on a zig-zag movement of the collector, and their fiber morphology (such as period and amplitude) could be broadly adjusted (Fig. 2d) [43]. Taking advantage of this approach, multi-material serpentine scaffolds can be constructed using a multi-nozzle using 3D printing system (Fig. 2e) [44].

In addition, the interactions between the fibers and the substrate type can influence the fiber deposition accuracy. For example, Hou et al. found that using an aluminum foil with a 45° relative placement angle resulted in the smallest fiber deposition deviation ratio of less than 1.16% [36]. Furthermore, multi-biomaterial fibrous scaffolds on non-flat surfaces were explored by maintaining a constant distance between the nozzle and the collector to ensure a

stable electrical field (Fig. 2f) [45]. Besides common flat substrates, mandrel collectors are commonly employed for constructing tubular scaffolds, which are extensively used in heart valves engineering and vascular grafts (Fig. 2g) [34, 46–48].

The printing accuracy of MEW is affected by various factors. The factors impacting the printing accuracy mainly include fiber deviation (including fiber overlapping and tilting) and residual charge densities [49]. Specifically, fiber deviation is influenced not only by processing parameters, such as material temperature, collector temperature, collector conductivity, applied voltage, and nozzle-to-collector distance, but also by scaffold design parameters and the inevitable presence of jet lag, including fiber diameter, layer number, and inter-fiber distance [50, 51]. Chang et al. introduced a post-process index (I_p), which compares the experimental proportion of void area in a top-view image of the fabricated scaffold sample (P_f) to the theoretical proportion in the scaffold design pattern (P_t), defined as $I_p = P_f/P_t$ (Fig. 2h). It is concluded that when I_p is equal to 1, the printing precision can be improved by reducing the fiber diameter and layer number, and increasing inter-fiber distance [51]. This phenomenon has been previously investigated, leading to the conclusion that a uniform fiber arrangement can be achieved when fiber spacing is five times greater than the fiber diameter (Fig. 2i) [52].

Although the above stacking deviation is considered inaccuracy, researchers can achieve precise control over geometry and mechanical properties by leveraging micro-scale layer displacement. This advancement allows for the creation of innovative nonlinear geometries, such as overhangs (Fig. 2j1) and branches (Fig. 2j2), as well as seamless transitions and abrupt changes in print tracks. These capabilities showcase the unparalleled flexibility of MEW [53–55].

3 Polymer Materials for Melt-Electrowriting

Table 1 lists the biomaterials commonly used by MEW in the field of tissue engineering and regeneration in recent years. In general, due to the nascent stage of MEW development and the scarcity of printable polymers, polycaprolactone (PCL) and its derivatives continue to dominate as the primary polymers [29]. PCL boasts exceptional biocompatibility, a high molecular weight, a low melting temperature, rapid solidification, and superb processing capabilities [56]. Moreover, PCL maintains its Young's modulus, yield strength and crystallinity under heated conditions for hours or days [57, 58].

Researchers can use various methods to modify the performance of PCL to meet the requirements of different tissue engineering applications. First, MEW PCL scaffolds exhibit low hydrophilicity which affects the cell adhesion/proliferation [59]. To address this issue, researchers have explored various post-treatment methods, including oxygen plasma treatment [58] and surface modification [60]. These methods significantly enhance the hydrophilicity of PCL scaffolds and the adhesion ability of cells. Second, researchers have mixed molten PCL with nano-hydroxyapatite (nHA) to fabricate PCL/nHA composite scaffolds to promote bone formation [61]. In addition, PCL and other materials were dissolved in certain organic solvents. After the solvent evaporates, PCL-based printing materials with specific functions are obtained. For example, PCL, polyethylene glycol (PEG), and roxithromycin (ROX) were mixed in tetrahydrofuran and subsequently evaporated. The MEW composite scaffolds exhibited improved hydrophilicity, cell proliferation, and antibacterial properties [62]. Similarly, PCL/magnesium phosphate (MgP) composite scaffolds exhibit significant potential for periodontal regeneration, while poly(hydroxymethylglycolide-*co*-ε-caprolactone) (pHMGCL)/PCL composite scaffolds demonstrate tunable degradation profiles and mechanical adaptability for cardiac tissue engineering applications [63]. In addition, a porous scaffold fabricated by poly(ε-caprolactone)-block-poly (ethylene glycol)-block-poly(ε-caprolactone) (PCEC) has been integrated with gelatin methacryloyl (GelMA) hydrogels to synergistically enhance their mechanical properties. The biocompatible triblock copolymer PCEC exhibited improved hydrophilicity and degradability compared to pure PCL [64].

Other materials have gradually come into view in recent years. Notably, PLA and poly(L-lactic acid) (PLLA) have been employed in the fabrication of high-fidelity structures [65, 66]. PLA and PLLA were widely used in tissue engineering and bone fixation, because they possess better biodegradability and high stiffness compared to PCL [67, 68]. Furthermore, poly(L-lactide-co-ε-caprolactone-co-acryloyl carbonate) (PLACLAC), synthesized via open-loop polymerization, has demonstrated efficacy in fabricating fibrous scaffolds with robust mechanical properties, including rigidity, elasticity, and creep resistance, specifically engineered for tendon and ligament repair [42].

4 Melt-Electrowriting Scaffolds for Tissue Engineering Applications

The onset of pathologies is frequently linked to disruptions in the ECM, leading to pathological tissue remodeling and ultimately tissue dysfunction [92, 93]. Previous studies have demonstrated considerable efforts in the domains of tissue engineering and regenerative medicine, highlighting the significance of replicating the intricate architecture of

Table 1 Polymers for MEW

Polymer	Printing conditions[a]	Structure[b]	Refs., Year
PCL	*22 G, 8 kV, 2.5 bar, 80 ℃, 300 mm/s*	Box, D = 20 μm	[32], 2022
	24 G, 3.5 kV, 0.2 bar, 90 ℃, 500 mm/min	Sinusoidal, D = 12.9 μm	[69], 2023
	4.5 kV, 1 bar, 85–90 ℃, 4.5 mm/s	Hexagonal, D = 15 μm	[70], 2018
	22 G, 7 kV, 0.8 bar, 90 ℃, 6 mm/s	Box, D = 20 μm	[71], 2022
	25 G, 6 kV, 0.22 bar, 85 ℃, 6 mm/s	Auxetic, D = 120 μm	[60], 2020
	340 μm, 3 kV, 30 μL/h, 75 ℃, 50 mm/s	Layer specific fiber orientations, D = 9.5 μm	[72], 2019
	21 G, 5–7 kV, 20 mL/h, 80 ℃	Gradient, D = 16 μm	[73], 2019
	24 G, 8.14 kV, 1.26 bar, 80 ℃, 8 mm/s	Box, D = 9 μm	[74], 2022
	21 G, 10 kV, 10 kPa, 90 ℃, 17 mm/s	Box, D = 4 μm	[75], 2019
	24 G, 10 kV, 0.06–0.08 MPa, 100 ℃, 40 mm/s	Box, D = 7 μm	[76], 2022
	5 kV, 0.4 bar, 80 ℃, 166 mm/min	Box, D = 10.9 μm	[77], 2023
	21 G, 1.5 kV, 0.1 MPa, 65 ℃	Box, D = 12 μm	[78], 2020
	23 G, 5.5 kV, 3 bar, 90 ℃	Box, D = 20 μm	[79], 2022
	23 G, 9.5 kV, 0.9 bar, 74 ℃, 1200 mm/min	Box, D = 9 μm	[80], 2022
	23 G, 5.6 kV, 0.7 bar, 85 ℃, 900 mm/min	Tubular, D = 21 μm	[81], 2023
	23 G, 4 kV, 0.025 MPa, 80 ℃, 280 mm/min	Tubular, D ≈ 14 μm	[46], 2024
	23 G, 8 kV, 180 kPa, 75 ℃, 1000 mm/min	Aligned, crimped and random, D = 20 μm	[82], 2020
	33 G, 2.9 kV, 2.8 bar, 109 ℃, 5500 mm/min	Box, D = 817 nm	[38], 2015
	23 G, 9.5 kV, 0.9 bar, 74 ℃, 1200 mm/min	Box, D = 8.7–9.2 μm	[80], 2022
	26 G, 7 kV, 0.07 MPa, 90 ℃, 40 mm/s	Box, D = 2.3 μm	[83], 2023
	11 kV, 0.15 MPa, 80 ℃, 1100 mm/min	Box, D = 15 μm	[84], 2023
	26 G, 7 kV, 0.07 MPa, 90 ℃, 40 mm/s	Box, D = 2.3 μm	[85], 2021
	150 μm, 3.2 kV, 1100 mbar, 90 ℃, 8 mm/s	Parallel microfibers, D = 25 μm	[52], 2023
	20 G, 3.5 kV, 0.25 bar, 70 ℃, 2000 mm/min	Box, D = 15 μm	[86], 2020
	25 G, 6 kV, 3 bar, 80 ℃	Box, D = 6 μm	[87], 2020
	25 G, 6 kV, 3 bar, 80 ℃	Mesh, D = 9.7 μm	[88], 2019
	23 G, 6.5 kV, 2 bar, 800 mm/min	Diamond, D = 9.44 μm	[89], 2025
	5 kV, 40 mbar, 90 ℃, 15 mm/s	Diamond, D ≈ 13 μm	[90], 2025
PCL + nHA	*340 μm, 3 kV, 10 μL/h, 70 ℃, 30 mm/s*	Box, D = 8.85 μm	[61], 2016
PHMGCL/PCL	*27 G, 7 kV, 2 bar, 84 ℃, 5 mm/s*	Box, D = 4–7 μm	[91], 2017
PLA	*200 μm, 2 kV, 1.8 kPa, 180 ℃, 100 mm/min*	Box, D = 10–20 μm	[65], 2023
PLLA	*3 kV, 0.1 MPa, 190 ℃, 15 mm/s*	Box, D = 29 μm	[66], 2022
PCL/PEG/ROX	*45 G, 2.3–2.6 kV, 1.5–3 kPa, 95 ℃, 10–20 mm/s*	Box, D = 6 μm	[62], 2020
PCEC	*28 G, 3.0–3.5 kV, 0.5 bar, 90 ℃, 2400 mm/min*	Layer specific fiber orientations, D = 400 μm	[64], 2021
P(ε-CL-co-AC)	*Straight fibers: 30 G, 7 kV, 1 bar, 55 ℃, 300 mm/min; Sinusoidal fibers: 30 G, 5.5 kV, 4 bar, 55 ℃, CTS*	Sinusoidal and straight, D = 26.8 μm	[42], 2018
PCL/MgP	*23 G, 7 kV, 80 kPa, 100 ℃, 5 mm/s*	Box, D = 60 μm	[63], 2023

[a]Nozzle size (*G, μm*), applied voltage (*kV*), air pressure/flow rate (*bar*/*kPa*), heating temperature (℃), collector speed (*mm/min, mm/s*)

[b]D: fiber diameter

native tissue. These biomimetic structures offer a promising avenue for the creation of functional tissue substitutes that can expedite the healing process [56]. Given that the collagenous fibers within each tissue exhibit distinct structures, all human tissues possess unique mechanical properties crucial for their functionality.

Advancements in MEW and biomaterials research have furnished the methodological and theoretical frameworks necessary for the implementation of biomimetic scaffolds. MEW enables the easy regulation of mechanical properties (such as the effective stiffness and anisotropy) of scaffolds. This capability allows for tailored designs that cater to

tissues with varying sizes or structures. Hence, this strategy has been widely employed to fabricate scaffolds with microscale fibrous structure for tissue engineering applications (Table 2).

This section discusses the specific applications of MEW scaffolds in tissue engineering and systematically covers the main application fields, highlighting the unique challenges and demands of different tissues, etc. This section will successively explore the application progress and challenges of MEW scaffolds in the fields of cardiac tissue engineering, bone regeneration, cartilage tissue engineering, vascular grafts, ligament and tendon tissue engineering, periodontal regeneration and nerve repair.

4.1 Cardiac Tissue Engineering

Cardiovascular diseases (CVDs) have high morbidity and mortality rates, often leading to extensive myocardial cell loss in the left ventricle, which is subsequently replaced by fibrotic scar tissue [94, 95]. This scarred area loses its contractile ability, ultimately leading to heart failure [96]. Adult myocardial tissue has limited regenerative capacity, often leading to progressive pathological remodeling as the heart attempts to compensate for lost contractility [97].

Reconstructing cardiac tissue in vitro represents a potential strategy for treating myocardial tissue loss. This strategy lies in replicating the fibrous structure and mechanical environment of native cardiac tissue, which includes appropriate mechanical performance to facilitate contraction, the ability to guide the orientation of cell alignment, and outstanding conductivity to promote electrical signal propagation between myocardial cells [98]. Moreover, the conductive scaffold can promote synchronous contraction and the expression of proteins involved in muscle contraction and electrical coupling [99, 100].

Previous research has shown that the stiffness of heart muscle is approximately 10–20 kPa at the beginning of diastole, increasing to 50 kPa in a healthy heart by the end of diastole, and can reach 200–300 kPa in an infarcted heart; the passive strain of the myocardium can reach 15–22%, and the myocardial conductivity is approximately 0.57 S/m. By carefully integrating these prerequisites, researchers can develop innovative methods to address the potential loss of myocardial tissue, offering new hope for the treatment of CVDs and heart failure [101–103].

4.1.1 MEW Scaffolds for Cardiac Tissue Engineering

Various melt MEW scaffolds have been developed, and extensive research has focused on their mechanical properties. The most common design is grid structure, which exhibits isotropic mechanical properties. In contrast, the rectangular structure (Fig. 3a) exhibits anisotropic properties depending on its aspect ratio, providing flexibility in adjusting mechanical properties through precise manipulation of the aspect ratio [32, 91]. However, it is crucial to note that the long-term mechanical performance of these scaffolds as implants has not been thoroughly evaluated.

To achieve synchronized deformations and long-term implantation, it is essential to design scaffolds that possess suitable mechanical properties. Chen et al. developed a fibrous scaffold with sinusoidal structures under specific printing conditions below the CTS (Fig. 3b). This structure has a smaller period than the serpentine structure (Fig. 3c) [44], so it can regulate cell behavior at the cellular scale. When stretched with constant frequency and strain, sinusoidal scaffolds exhibited a lower Young's modulus and a higher elastic limit strain compared to rectangular scaffolds, which is beneficial for synchronized contraction of beating cells. Moreover, MEW shows the flexibility of adjusting the anisotropy ratio of sinusoidal scaffolds [69]. Notably, the sinusoidal mesh could extend along its long axis by up to 23% before undergoing irreversible deformation, compared to 7% for straight fibers. The elastic strain energy of sinusoidal scaffolds was more than three times higher than that of rectangular grids. Analogously, the serpentine architectures can mimic the curved collagenous fibers in the cardiac ECM, and the scaffolds show outstanding flexibility and elasticity compared with straight ones [43]. This structure is more path-dependent, and therefore, more controllable than sinusoidal structures constructed below the CTS.

Another interesting structure is the auxetic structure (Fig. 3d), which can be considered as a macroscopic version of the sinusoidal structure [60]. Unlike the microscale sinusoidal structure, auxetic structures exhibit bidirectional simultaneous deformation based on a negative Poisson's ratio. This leads to expansion in multiple directions simultaneously and enhances unique properties, such as shear resistance, indentation resistance, and synclastic curvature, making it an attractive option for cardiac patches [103]. Inspired by beehives, Castilho et al. generated fibrous scaffolds with hexagonal 3D microstructures that can achieve large and anisotropic reversible deformations (Fig. 3e). These scaffolds demonstrated potential for minimally invasive applications and were able to extend along the x-direction by 35%–40% before permanent deformation, compared to 2%–3.5% for rectangular scaffolds. Notably, the energy absorption and release capacity of hexagonal scaffolds during elastic deformation was 20–40 times greater than that of rectangular structures [70]. Furthermore, some latest research focuses on the combination of hydrogels and MEW scaffolds. For example, Vega et al. fabricated a bio-inspired scaffold with diamond-shaped pores by MEW, this geometry exhibited a large deformation beyond 50% in the short direction

Table 2 MEW of composite scaffolds and their function

Application	Matrix	Bioactive materials	Method	Geometric structure	Cell type	Effect	Refs., year
Cardiac tissue engineering	PCL	Matrigel	Embed	Squares	hiPSC–CMs	Promote hiPSC–CMs alignment and interconnectivity	[32], 2022
	PCL	Gold nanoparticles	Sputter coating	Sinusoidal	hiPSC–CMs	Enhance the electrical propagation and synchronous contraction of hiPSC–CMs	[69], 2023
	PCL	PPY	Situ chemical oxidative polymerization	Auxetic	MSCs	Support large deformation and electrical conduction	[60], 2020
	PCL	None	None	Sinusoidal	Primary rat CMs	Facilitate the beating behavior, gene expression, and accelerate the maturation of primary rat CMs	[43], 2024
	PCL	PVDF, Fe_3O_4	Multimaterial 3D printing platform	Serpentine	Primary rat CMs	Improve the maturation of cellular phenotype, and significantly improve the cellular structure, function, and gene expression, enhance the capabilities in repairing damaged ventricular structure and function in vivo	[44], 2024
	PCL	Collagen	Coated	Hexagonal	hiPSC–CMs	Supports significant biaxial deformation, promotes hiPSC–CMs maturation and cardiac repair	[70], 2018
	PCL	PEDOT:PSS–PEO	Layered printing	layer-specific fiber orientations	H9C2 cells and primary rat CMs	Promote the H9C2 cells specific arrangement and proliferation, and promote synchronous contraction of primary rat CMs	[72], 2019
	pHMGCL + PCL	Collagen	Coated	Rectangular	CPCs	Promote CPCs alignment along the rectangular long axis	[91], 2017
	PCL	None	None	Diamond	hiPSC–CMs	Enhanced maturation at the metabolic and bulk gene expression level	[89], 2025
	PCL	Fibrin	Consecutive hybrid bioprinting	Diamond	C2C12	Facilitate cell-induced anisotropic remodeling of fibrin filaments and the formation of highly aligned myoblast bundles along the bioprinting trajectory	[90], 2025
Bone regeneration	PCL	nHA	Chemical precipitation method	Square	MSCs	Promote bone formation and microvasculature formation	[71], 2022
	PCL	nHA	Mixture and solvent evaporation	Square	MC 3T3-E1	Promote cellular proliferation and alignment	[61], 2016
	PCL	None	None	Square	MSCs	The 100 μm pore size group promote MSC osteogenesis and differentiation	[75], 2019

Table 2 (continued)

Application	Matrix	Bioactive materials	Method	Geometric structure	Cell type	Effect	Refs., year
	PCL	CaP	Chemical precipitation method	Homogeneous, gradient and offset	hOB	Promote cell infiltration and growth	[73], 2019
	PCL	pHA, nHA HA	Chemical precipitation method, mixture and solvent evaporation	Square	MSCs	Promote MSCs osteogenesis, facilitate the binding, stabilization, and controlled release of BMP2 from the material	[126], 2020
	PCL	PEG, ROX	Mixture and solvent evaporation	Square	MG63	Enhance the hydrophilicity and antibacterial activity	[62], 2020
	PLLA	Gelatin and bioglass particles	Casted and crosslinking	Lattice	KUSA-A1	Facilitate nHA formation and promote bone formation	[66], 2022
Cartilage tissue engineering	PCEC	HA, GelMA, TGF-β1, and BMP-7	Hierarchical construction: microspheres packaging, UV crosslinking, and casted	Tri-layered composite scaffolds	MSCs	Facilitate the regeneration of both cartilage and subchondral bone	[64], 2021
	PCL	None	None	Square	MSCs	Promote the formation of scalable tissues with a spatial collagen fiber organization	[76], 2022
	PCL	TGF-β1	APPJ	Square	MSCs	Promote chondrogenic differentiation and neo-cartilage matrix production	[74], 2022
	PCL	None	None	Square	hPDCs	Promote up-regulation of chondrogenic and prehypertrophic gene markers	[77], 2023
	PCL	TGF-β1, BMP-7, IGF-1, and HA	Hierarchical construction: microspheres packaging	Square	MSCs	Filled the injury site and promoted partial repair of the injury	[78], 2020
	PCL	NorHA hydrogels	Structure embedding and hydrogel crosslinking	Square	MSCs	Support MSC chondrogenesis and neocartilage formation	[79], 2022
Vascular	PCL	None	None	Microporous	HUASMCs	Guided cellular attachment and subsequent ingrowth	[81], 2023
	PCL	None	None	Sinusoidal	HUVECs	Supply substrates for cellular attachment and growth in vitro, achieve biomimetic performance	[46], 2024

Table 2 (continued)

Application	Matrix	Bioactive materials	Method	Geometric structure	Cell type	Effect	Refs., year
	PCL	None	None	Diamond, auxetic, closed cell, and open cell	None	Enhance the tensile properties	[48], 2022
Ligament and tendon tissue engineering	PCL	None	None	Crimped	MSCs	Guide cell orientation and improve mechanical resilience	[82], 2020
	P(ε-CL-co-AC)	None	None	Sinusoidal, straight	L929, MSCs	Improve mechanical performance	[42], 2018
Periodontal Regeneration	PLGA/GEL	Cu@MSNs	Mixture	Bi-layered	MSCs, L929	Support osteogenic and antibacterial properties	[154], 2020
	PCL	F/CaP	Chemical precipitation method	Tissue specific	hPDLCs	Guide tissue-specific stem cell differentiation and macrophage polarization	[83], 2023
	PCL	None	None	Biphasic construct	hPDLCs	Guide collagen attachment, extend, and infiltrate, mimic PDL regeneration	[80], 2022
	PCL	MgP	Mixture and solvent evaporation	Graded scaffolds	MSCs	Support in vitro mesenchymal stem cell differentiation toward the osteoblastic lineage and in vivo bone regeneration, partitions coordinated bone and periodontal tissue regeneration	[63], 2023
	PCL	CaP	Chemical precipitation method	Biphasic construct	hPDLCs	Promote periodontal regeneration	[84], 2023
	PCL	F/CaP	Chemical precipitation method	Square	hPDLCs	Enabling the differentiation of resident progenitor cells, guide the coordinated growth of soft and hard periodontal tissues, and supply antimicrobial properties	[85], 2021
Nerve repair	PCL	None	None	Microfibrous architecture	C2C12	Guide cellular alignment, enhance cellular migration, and accelerate the outgrowth of neurites	[52], 2023
	PCL	Gold nanoparticles	Sputter coating	Square mesh	PC12	Promote neurite outgrowth and electrical signal transmission	[86], 2020
	PCL	None	None	Square	Mouse cortical neurons	Enhance cell viability and the neuronal network maturation	[87], 2020
	PCL	None	None	Square	Ltk-11	Construct 3D system to mimic physiological tissue environment, guide cell migration and provide physical cues	[88], 2019
	PCL	PPY	Situ chemical oxidative polymerization	Square mesh	SH-SY5Y neurons (ATCC)	Supporting growing axons in extending through the spinal cord lesion site	[163], 2024

(Fig. 3f). Moreover, the flexible scaffold was encapsulated within a fibrin-cell hydrogel suspension, which exhibited a high cell density and thereby enabled large-scale synergistically deformation of the scaffold [89]. Qiu et al. utilized a consecutive hybrid bioprinting strategy by combining MEW and extrusion-based bioprinting to construct oriented tissues on the fibrous scaffold. The resultant aligned myoblast constructs could be differentiated into multinucleated myotubes with enhanced muscle-specific protein and gene expression [90].

In summary, diamond, hexagonal, auxetic, and sinusoidal structures demonstrate superior mechanical behavior compared to rectangular scaffolds. Their enhanced elastic response and higher failure strain facilitate synchronized cardiac tissue contraction. Furthermore, these studies emphasize the significant potential of MEW in constructing fibrous scaffolds with tailored structure and mechanical properties to meet the requirements of cardiac tissue.

4.1.2 Electrically Conductive Functionalization of MEW Scaffolds

Endowing MEW scaffolds with suitable conductivity can significantly enhance signal propagation for cardiomyocytes (CMs) [98]. Conductivity is a crucial evaluation criterion for cardiac fibrous scaffolds. Over the past decades, advancements in the modification of conductive materials on the MEW scaffolds have primarily centered around three methods: sputter coating [69], *in-situ* chemical oxidative polymerization [60], and hybrid printing [72].

During sputter coating, a thin layer of gold nanoparticles is deposited onto PCL scaffolds. When subjected to high-intensity electrical fields, these scaffolds demonstrated a significant increase in their ability to coordinate synchronous contractions between cardiac cells after 120 h of electrical stimulation [69]. However, compared to sputter coating, scaffolds modified with polypyrrole (PPy) through *in-situ* chemical oxidative polymerization exhibit superior conductivity and enhanced chemical stability (Fig. 3g) [60].

Moreover, hybrid EHD printing presents an alternative approach to achieving conductive functionality. This method allows for the construction of a poly(3,4-ethylenedioxythiophene)–poly(styrenesulfonate)–polyethylene oxide (PEDOT:PSS–PEO) conductive layer that mimics the multiscale, layer-specifically oriented architectures of native myocardium in a controlled manner (Fig. 3h) [72].

Beyond conductive materials, piezoelectric materials have gradually gained significant attention with the advancement of electroactive materials [104]. A recent study demonstrated multimaterial-printed serpentine microarchitectures comprising PCL fibers, polyvinylidene fluoride (PVDF) fibers, and PCL/Fe_3O_4 magnetic microfibers (Fig. 3i). PCL microfibers were used as mechanical support and PVDF microfibers were used for piezoelectric stimulation. The magnetic deformation of the multi-material structure was controlled by an external magnet through PCL/Fe_3O_4 fibers. This engineered piezoelectric cardiac scaffold shows significant structural and functional repair of infarcted myocardium, demonstrating the therapeutic potential of piezoelectric cardiac structures in the treatment of myocardial infarction [44].

4.2 Bone Regeneration

Bone tissue engineering scaffolds can provide effective strategies for bone injury repair and replacement, such as osteoporosis, osteonecrosis, and osteomalacia [105, 106]. These scaffolds can replicate the natural bone ECM, promoting the adhesion, proliferation, and differentiation of bone cells [107–109]. In recent years, progress has been made in the creation of bone tissue engineering scaffolds capable of providing essential osteoconductive and osteoinductive cues that support robust bone regeneration [110, 111]. Various methods have been employed to fabricate these scaffolds, including lyophilization [112], solution electrospinning [113], and additive manufacturing techniques [114]. Among these methods, MEW has the ability to fabricate high-resolution biomimetic fibrous structures in a controlled manner, and its microarchitecture plays a pivotal role in regulating bone healing response.

4.2.1 MEW Scaffolds for Bone Tissue Engineering

During the process of bone healing, the formation of new blood vessels is a key connection in the repair. They promote bone tissue reconstruction by providing oxygen, nutrients and cellular support. MEW scaffolds can support the growth of smaller vascular networks during bone repair, primarily composed of vessels with diameters at or below 20 μm [115]. Moreover, FDM scaffolds have been introduced to promote bone regeneration. These scaffolds feature a 0°/90° lay-down pattern and possess exceptional biomechanical properties, and the large pores of FDM scaffolds can facilitate the development of larger vessels [116, 117]. Kelly et al. investigated how scaffolds' microstructures in FDM and MEW affect the healing of large bone defects. The results revealed that FDM PCL scaffolds facilitated the formation of large bone spicules through their pores, whereas MEW PCL scaffolds contributed to the development of a rounder bone front during the healing process. Furthermore, both FDM and MEW scaffolds demonstrated the ability to support vascularization, FDM scaffolds supported greater total vessel formation, including the development of larger vessels (Fig. 4a) [71]. Compared with FDM scaffolds, MEW

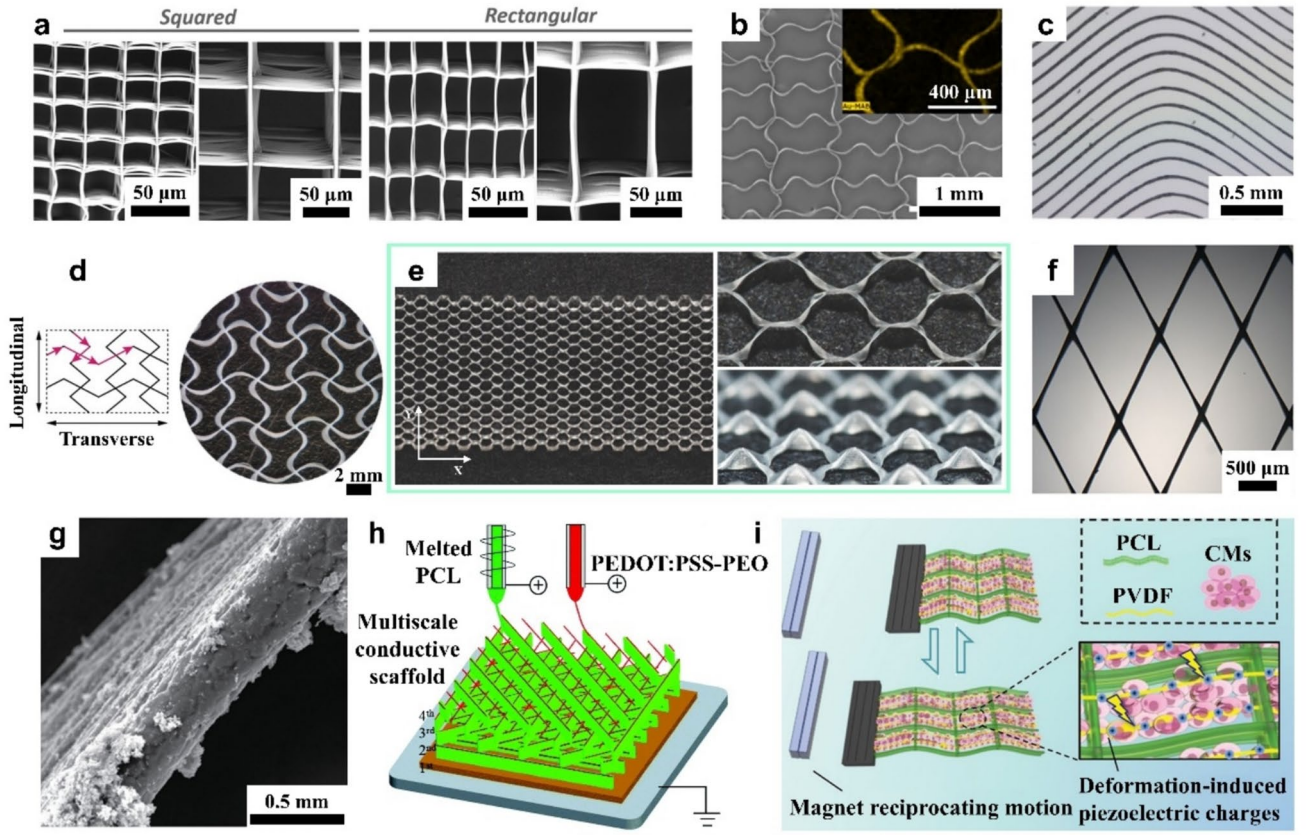

Fig. 3 MEW scaffolds for cardiac tissue engineering. **a** Squared and rectangular MEW microfibrous scaffolds; Reproduced with permission from Ref. [91], Copyright 2017, Wiley–VCH. **b** Sinusoidal scaffolds printed at print speeds below CTS; Reproduced with permission from Ref. [69], Copyright 2023, Elsevier. **c** Sinusoidal PCL fibers with a period of 3 mm and an amplitude of 2 mm; Reproduced with permission from Ref. [43], Copyright 2024, American Chemical Society. **d** Printing path and structure morphology of auxetic structure; Reproduced with permission from Ref. [60], Copyright 2020, Wiley–VCH. **e** MEW scaffolds with hexagonal cells structure; Reproduced with permission from Ref. [70], Copyright 2018, Wiley–VCH. **f** Image of full scaffolds printed under final conditions: *6.5 kV, 800 mm/min, 2 bar*; Reproduced with permission from Ref. [89], Copyright 2025, Wiley–VCH. **g** Morphology of PPy modified on fibrous scaffolds before and after; Reproduced with permission from Ref. [60], Copyright 2020, Wiley–VCH. **h** Schematic of the fabrication of multiscale conductive scaffolds; Reproduced with permission from Ref. [72], Copyright 2019, Royal society of chemistry. **i** Schematics of magnet-driven mechanical and piezoelectric stimulation for cardiac maturation; Reproduced with permission from Ref. [44], Copyright 2024, Wiley–VCH

scaffolds supported higher levels of new bone formation and encouraged the formation of a dense microvascular network with minimal infiltration of larger vessels into the defect area.

Recreating the biomimetic structure of bones holds immense potential for treating bone injuries and diseases. Researchers have demonstrated that pore sizes of 100 µm and larger are conducive to bone formation. This is attributed to their high global stiffness, local fiber stiffness, superior seeding efficiency, ability to maintain a spread cellular morphology, and significant enhancement of human mesenchymal stromal cells (MSC) collagen and mineral deposition [75, 118]. However, pore sizes exceeding 500 µm also enhance vascularization and bone formation through their large surface areas and excellent interconnectivity [119]. High specific surface areas offer numerous benefits, including optimal cell attachment, increased protein adsorption sites, potential enhancement of the ligand density available for cell binding, and improved oxygen delivery [120–122]. Notably, offset and 250 µm homogeneous scaffolds can provide these capabilities (Fig. 4b). In addition, porous scaffolds with a porosity-graded architecture serve as an excellent template for mimicking the natural bone ECM [73].

Significant progress has been made in recent years in the design and biomaterials employed for bone regeneration. Various biomaterials, such as PCL, PLLA, and poly(lactic–co-glycolic acid) (PLGA), have been dedicated to fabricate bone tissue engineering scaffolds. The application of PLLA scaffolds is limited due to their lack of flexibility and relatively low biological activity [123].

To overcome these limitations and create natural bone ECM environment, Xu et al. fabricated a MEW PLLA lattice/gelatin/bioglass reinforced scaffold with a controllable interconnected porous architecture (Fig. 4c). This composite scaffold exhibited an enhanced storage modulus and an exceptional ability to form apatite crystals in vitro [66].

4.2.2 The Combination of MEW Scaffolds with Bioactive Materials to Promote Bone Repair

Recreating the mineral environment of bone holds immense potential for treating bone injuries and diseases. Studies have shown that the mineral structure of bone consists of needle-shaped mineral units that aggregate to form an irregular 3D nanoscale structure. These unique topographies endow bone with exceptional biological and mechanical properties [124].

To achieve this nanoscale structure and promote bone healing, nHA was coated onto various scaffolds (Fig. 4d). The resultant scaffolds promote osteogenic differentiation and polarize human macrophages toward an M2 phenotype, thereby enhancing the production of anti-inflammatory cytokines, such as IL-10 [125–127]. In addition, calcium phosphate (CaP), another common biomaterial that resembles the inorganic mineral phase crystals found in bone, can modulate osteoclast and osteoblast activity by releasing calcium and phosphorus ions (Fig. 4e) [73]. The modification of these biomaterials created an environment conducive to bone growth which improves the infiltration, proliferation, and attachment of osteoblasts on the scaffolds.

The chemical precipitation method is a prevalent technique for modifying the mineral composition on the surface of MEW scaffolds by integrating PCL fibers and functional materials. For instance, to circumvent surgery-induced bone infection, which may hinder bone repair and regeneration, ROX was incorporated into fibrous scaffolds. The results demonstrated that PCL/PEG/ROX scaffolds exhibited an initial burst drug release followed by sustained long-term release, which is beneficial for preventing and treating bone infections [62].

Furthermore, composite scaffolds can enable effective biomimetic functionalization [128]. To enhance the flexibility and relatively low biological activity of PLLA, Xu et al. combined the MEW PLLA scaffold and gelatin/bioglass underwent chemical changes, with the amino (NH^{3+}) groups of the gelatin molecular chain serving as active sites for the formation and induction of nHA crystal growth. As the $COO^{-}/Ca^{2+}/COO^{-}$ ionic bonding extended, phosphoric ions (PO_4^{3-}) were incorporated to promote the nucleation of nHA [66].

4.3 Cartilage Tissue Engineering

Articular cartilage is capable of bearing high and regular loads, which can effectively protect the ends of articulating joints for decades under normal physiological conditions [129, 130]. However, damage to articular cartilage accelerates joint degeneration and leads to osteoarthritis, but its regenerative capacity is extremely limited [131, 132]. The construction of engineered artificial cartilage analogues primarily requires two essential prerequisites: simulating the regional structure of natural cartilage (the superficial layer, transition layer, and deep layer), and the incorporation of cartilage growth factors [133]. The former endows the tissue with load-bearing capacity through collagen fiber arrangement and proteoglycan distribution, while the latter promotes the differentiation of chondrocytes and tissue formation [134–136].

Currently, cell-based strategies are the most common methods for treating articular cartilage defects. However, they often lack suitable structural support and result in poor long-term implantation performance [137]. MEW has been widely used to construct a network that supports cell proliferation and differentiation, effectively recapitulating the structure of natural cartilage and enabling it to support regular load-bearing activities [138].

4.3.1 MEW Fibrous Scaffolds for Cartilage Implants

To improve the structural organization of engineered cartilage tissues, researchers have combined the benefits of cellular self-assembly with MEW printed fibrous scaffolds [139]. These scaffolds can be used to guide the deposition of a biomimetic collagen network within engineered tissue, mimicking the structure and function of native articular cartilage. Furthermore, several key metrics are considered to evaluate the mechanical properties of these scaffolds: the equilibrium modulus, dynamic modulus, compression modulus, and Young's modulus [140].

Guidance on these mechanical properties provides a guideline for researchers in the field of engineered cartilage analogues. One such innovation involves the use of MEW scaffolds to enhance the mechanical properties of hydrogels (Fig. 5a). This innovative strategy synergistically integrates the hydrogel that contribute to regional regulation of cell fate and MEW fibrous scaffolds-facilitated modulation of adhesion, proliferation, and differentiation. Notably, this approach demonstrates considerable potential for alternative implants and achieves native cartilage-like mechanical properties [64]. The advantage of MEW can also be used to fabricate sophisticated bilayered microfibrous architecture which can duplicate the zonal mechanical properties of articular cartilage (Fig. 5b)

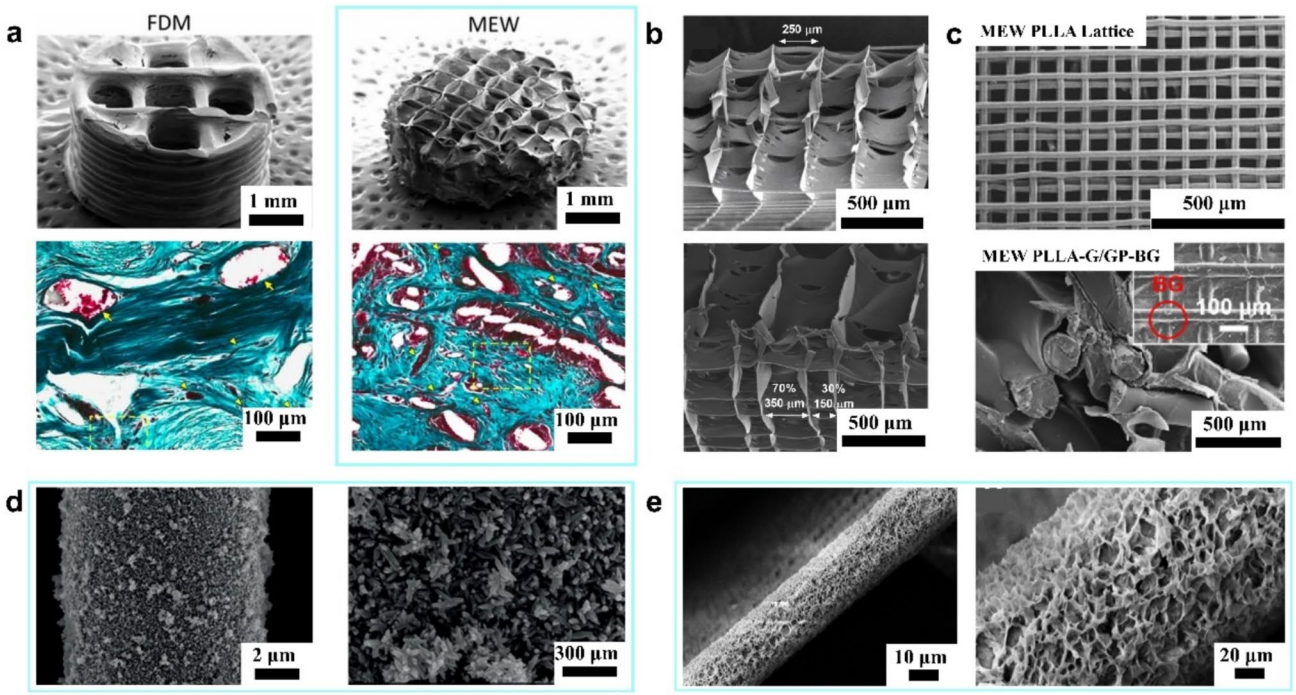

Fig. 4 MEW scaffolds for bone regeneration. **a** FDM and MEW scaffolds after 21 days of human MSCs; Reproduced with permission from Ref. [71], Copyright 2022, IOP Publishing Ltd. **b** Different pore-structured PCL scaffolds fabricated by MEW; Reproduced with permission from Ref. [73], Copyright 2019, American Chemical Society. **c** Composite scaffolds composed of MEW PLLA lattice and gelatin/genipin/bioglass hydrogel; Reproduced with permission from Ref. [66], Copyright 2022, Elsevier. **d** PCL fibers modified with mineral nanostructure; Reproduced with permission from Ref. [126], Copyright 2020, Wiley–VCH. **e** PCL fibers modified with CaP; Reproduced with permission from Ref. [73], Copyright 2019, American Chemical Society

[141]. Moreover, hybrid bioprinting provides a versatile and scalable approach for biological joint resurfacing, in which inkjet printing was used to deposit numerous cells into MEW scaffolds that can self-assemble into an ordered array of spheroids, finally generating a hybrid tissue (Fig. 5c). By employing this method, the scaffold exhibited impressive equilibrium moduli, reaching 180 kPa and 214 kPa at 20% and 30% strain, respectively. These values are indicative of the compressive stiffness of the tissue's solid matrix and are comparable to those of native tissue (0.2–2 MPa). The tensile Young's modulus of the engineered cartilage was 1.4 MPa, approaching the range of native cartilage (5–12 MPa) [76]. Furthermore, the porous structure of these scaffolds can serve as a cell collector, facilitating the construction of cartilaginous scaffolds and enhancing gene expression associated with chondrogenesis [77].

4.3.2 Functionalization of MEW Scaffolds with Chondrogenic Factors

Cartilage growth factors hold immense potential in promoting cartilage formation and development. The incorporation of chondrogenic growth factors within bio-scaffolds architectures enables promote the formation of cartilage while recapitulating the multifaceted functional characteristic of native cartilage.

Cytokines, such as transforming growth factor-β (TGF-β), exert a profound influence on chondrogenic differentiation throughout developmental stages, maintaining chondrocyte quiescence and preventing hypertrophy. Thus, the strategy of immobilizing TGF-β onto MEW PCL polymers has shown promise in supporting chondrocyte differentiation and facilitating cartilage tissue formation. In a previous study, a novel atmospheric-pressure plasma (APPJ) surface treatment method was explored, which allows for the covalent immobilization of TGF-β onto 3D-printed polymeric meshes. This surface modification technique enhances protein loading efficiency and bioactivity while preserving mesh strength and fostering chondrogenic differentiation (Fig. 5d) [74, 142].

In addition, the combination of MEW fibrous scaffolds with hydrogels can significantly enhance the mechanical properties of hydrogels. Burdick et al. increased the modulus of soft norbornene-modified hyaluronic acid (NorHA) hydrogels by approximately 50 times using MEW scaffolds with a spacing of 400 µm while retaining the chondrogenic potential of the hydrogels. Moreover, NorHA hydrogels

demonstrated the capacity to enhance the cartilage formation and maturation [79].

4.4 Vascular Grafts

CVDs remain the leading cause of death worldwide, and the therapeutic schedule of CVDs mainly relies on the implantation of vascular grafts. The fabrication of vascular grafts should replicate the native vascular structure to facilitate cell penetration and possess suitable mechanical performance. Mimicking the mechanical properties of native blood vessels is crucial for maintaining graft patency and preventing hemodynamic failure [46]. A mismatch in radial mechanical compliance, particularly at the anastomosis site, can lead to intimal hyperplasia, ultimately resulting in graft failure. Furthermore, in the design of double-layer scaffolds, the inner layer can serve as an antithrombotic barrier, and the outer layer promotes the directional migration of cells and signal transmission through controllable fiber arrangement.

MEW is extensively utilized in the biofabrication of vascular grafts, particularly those with small diameters [143]. The fabrication of tubular grafts depends on cylindrical mandrels, deposited fibers are collected on a rotating mandrel with linear slide translation (Fig. 6a), tubular structures of various diameters can be fabricated using different-sized mandrels. The ability to fabricate tubular grafts with a low pore size and a high number of pivot points by controlling process parameters has been previously demonstrated (Fig. 6b) [34]. Moreover, achieving suitable printing parameters is essential to ensure the highest possible accuracy in pattern fabrication, such as minimizing jet lag by adjusting the printing speed to the CTS [144].

The MEW vascular grafts exhibit high reproducibility, minimal variation in fiber diameter, and negligible pore spacing deviation [46, 81]. Moreover, the MEW technique can adjust the mechanical properties of scaffolds by optimizing the microstructure of the scaffold. Previous research has established the impact of microstructure on the overall mechanical attributes of these grafts, such as the diamond, auxetic, closed cell (straight and wavy), and open cell (straight and wavy) (Fig. 6c) [48].

To evaluate the mechanical properties of vascular grafts, longitudinal and circumferential tensile tests are employed to assess uniaxial mechanical properties, facilitating the derivation of graft strength and elastic modulus based on the stress–strain response. These indirect testing methods can be used to estimate equivalent burst pressure, as the high porosity of MEW scaffolds renders them unsuitable for direct bursting pressure methods [145]. In addition, human arterial vessel burst pressures range from 1200 to 4200 mmHg, while arterial compliance ranges from 8.0% to 17.0% per 100 mmHg, these indexes can be used as reference standards for the design of vascular grafts [146, 147].

Grafts exhibiting better compliance tend to possess superior dynamic performance. The diamond and auxetic structures are typical structures with the above properties. The auxetic structure demonstrates a negative Poisson's ratio with bidirectional stretching, whereas the diamond structure undergoes radial contraction. In addition, significant differences are observed between open-cell (straight and wavy) and closed-cell structures in terms of elastic modulus. The closed-cell structure boasts higher stiffness with an elastic modulus of several MPa, compared to the open-cell structure, which falls within several kPa. Furthermore, the open-cell structure has a better deformability at the direction of longitudinal (up to 150%) compared to closed-cell structure. This exceptional deformation capability of the open-cell (straight and wavy) structure stems from the offset design of fibers parallel to the loading axis, with wavy fibers playing a less significant role compared to straight fibers.

Furthermore, pore spacing influences the overall mechanical performance of the grafts. Klein et al. investigated the production of highly porous, biocompatible microfibrous scaffolds featuring a sinusoidal microstructure (Fig. 6d). Their findings revealed that scaffolds with small-diameter sinusoidal structures and 250 μm spacing exhibited mechanical properties akin to native blood vessels and encouraging initial cell culture results. A similar trend was observed for strength and failure, suggesting enhanced mechanical performance in scaffolds with reduced pore spacing [46].

4.5 Ligament and Tendon Tissue Engineering

Tendon and ligament injuries are common worldwide, yet treatment remains challenging due to limited donor availability, healing complications, and frequent reinjury risks [148]. This drives the need for biomaterial-based replacements that can effectively restore damaged tissues. These connective tissues exhibit unique mechanical features including nonlinear stretching properties, highly aligned cell patterns, and wavy collagen fiber characteristics that are difficult to reproduce [82]. Collagen fibers serve dual roles by supporting tissue regeneration while maintaining mechanical stability, enabling the tissues to endure cyclic stretching during movement.

Recently, Groll et al. fabricated a robust, elastic, and creep-resistant sinusoidal scaffolds utilizing MEW, which exhibits enhanced mechanical properties after UV crosslinking (Fig. 7a) [42]. In addition, the scaffold has demonstrated cytocompatibility and the ability to mimic natural ligaments and tendons, the sinusoidal structure significantly enhanced the flexibility of this scaffold, enabling it to manage the loading and unloading of collagen fibers during movement (Fig. 7b) [82]. Meanwhile, the geometric morphology of the fibers can guide cells to align along the fiber path [149]. To further construct a biomimetic tendon

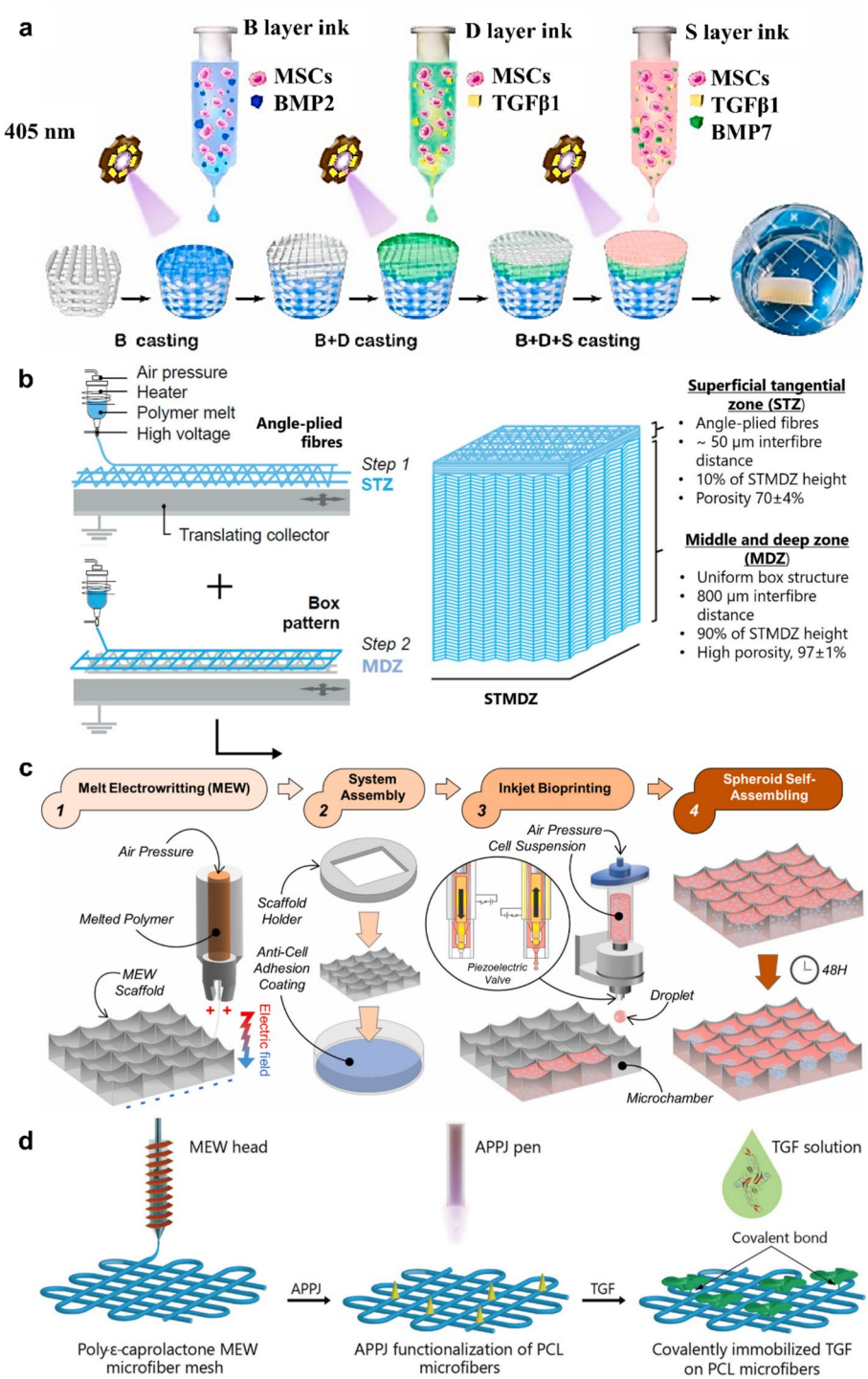

Fig. 5 MEW scaffolds for cartilage tissue engineering. **a** Integrated tri-layered composite scaffold was constructed using the UV-assisted, stepwise infiltration and crosslinking procedures. As shown, with the assistance of UV-crosslinking, the cell and growth factor-laden GelMA hydrogel precursor solution of the respective layer was successively infused into the fiber networks for the B, D and S layers to construct the tri-layered fiber-reinforced hydrogel composite; Reproduced with permission from Ref. [64], Copyright 2020, Elsevier. **b** Design approach and sequential MEW of the bi-layered fibrous scaffolds; Reproduced with permission from Ref. [141], Copyright 2019, Elsevier. **c** MEW and inkjet bioprinting were combined into a sequential biofabrication framework: a defined number of MSCs were inkjetted into box-like MEW scaffolds, which supported spontaneous cellular aggregation within each microwell; Reproduced with permission from Ref. [76], Copyright 2022, Elsevier. **d** Schematic illustration showing covalent immobilization of TGF on microfibrous scaffolds; Reproduced with permission from Ref. [74], Copyright 2022, Wiley–VCH

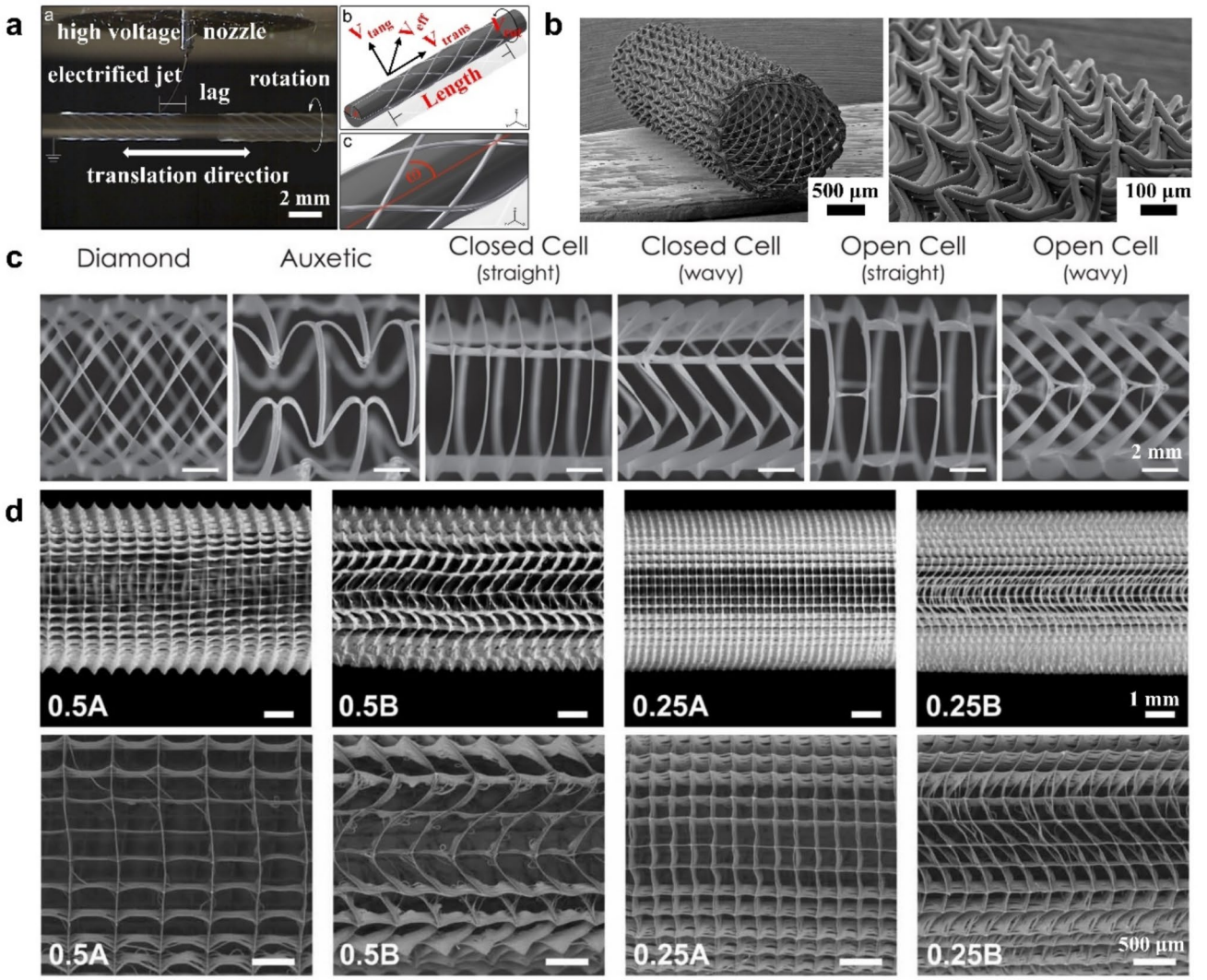

Fig. 6 MEW scaffolds for vascular grafts. **a** MEW vascular grafts fabricated by rotating mandrel; Reproduced with permission from Ref. [34], Copyright 2018, Elsevier. **b** Tube with a winding angle of 20° and 30 pivot points, with an internal diameter of 1.5 mm and wall thickness of approximately 200 μm; Reproduced with permission from Ref. [34], Copyright 2018, Elsevier. **c** Micrographs of printed tubular scaffolds for each of the six patterns. Scale bar = 2 mm; Reproduced with permission from Ref. [48], Copyright 2022, Wiley–VCH. **d** Morphology and geometric dimension of tubular PCL scaffolds (4.0 mm inner diameter) produced via MEW with varying architectural arrangements; Reproduced with permission from Ref. [46], Copyright 2023, IOP Publishing Ltd

structure, researchers have developed a multiscale scaffold with a hierarchical structure, which consists of a shell and a core (Fig. 7c). This biomimetic tendon exhibited strong tensile strength and the ability to accelerate the regeneration of tendon tissue [150].

4.6 Periodontal Regeneration

Periodontal disease refers to inflammatory pathologies affecting the periodontium (the specialized tissues supporting teeth), which arise from dysregulated host immune responses triggered by pathogenic microbial biofilms adhering to dental surfaces. Further loss of periodontal ligament (PDL) fibers may lead to loss of alveolar bone support after the destruction of connective tissue [151, 152]. Due to the complexity of periodontal tissue structure, tooth-supporting tissue regeneration is a complex clinical challenge [153]. In recent decades, significant efforts have been devoted to mimic the 3D structure of ligament-to-bone interfaces. This structure offers the advantage of hindering the migration of epithelial and connective tissues while providing an optimal environment for cell adhesion, proliferation, and osteogenic differentiation [154].

MEW scaffolds have been widely explored to replicate the 3D nanofibrous ECM of the PDL and bone compartment. The matrix of the PDL and bone compartment is

characterized by a parallel fibrous structure and pore size gradients (Fig. 8a) [83, 155]. The fibrous scaffolds facilitate cell and collagen alignment, relying on topographical cues and the fibrous structure to provide the necessary conditions for accelerated periodontal regeneration [80]. To reconstruct the interfaces of PDL and bone compartment, Malda et al. designed a novel graded scaffold comprising three distinct zones: a bone zone, an interfacial zone, and a PDL-to-bone zone (Fig. 8b). These graded composite scaffolds hold great application prospects in periodontal regeneration [63].

Different functional materials were coated on the scaffolds to enhance the osteogenic capacity. For example, CaP is widely employed to stimulate rapid bone regeneration (Fig. 8c). Given that tooth tissue comprises cementum and alveolar bone, materials that facilitate bone repair are equally applicable in dental contexts [84]. Notably, fluorinated calcium phosphate (F/CaP)-coated MEW PCL fibrous scaffolds not only expedite bone regeneration and foster concurrent regeneration of tooth–ligament–bone interfaces but also exert significant impact on *Porphyromonas gingivalis* (Fig. 8d) [83, 85]. Furthermore, the osteoconductive materials with the chemical composition can enhance bone regeneration. Among them, MgP bioceramics can promote bone regeneration ability (Fig. 8e) [63].

Given the microbially abundant oral environment and the scarcity of antibacterial biomaterials in clinical practice, Zhang et al. introduced an innovative method to encapsulate copper (Cu) within mesoporous silica nanoparticles (MSNs) to form a Cu-loaded MSNs (Cu@MSNs) bilayer scaffold. The resultant scaffold prevented interference from non-osteoblastic cells and offered the dual advantages of supporting bone ingrowth and inhibiting bacterial infections [154].

4.7 MEW Scaffolds for Nerve Repair

Peripheral nerve injury has always been difficult and challenging in clinic because of its complex physiological structure and uncontrollable pathophysiological process [156]. Nerve tissue damage, particularly when exceeding 5 mm in severity, can impair this conduction ability and hinder self-regeneration [157]. Autologous nerve transplantation has drawbacks, such as limited donors, donor function loss, neuroma formation, nerve deformation or dislocation, and mismatch in nerve diameter. In addition, acellular allograft requires long-term immunosuppressive therapy, which may increase the risk of infection [158]. Consequently, the implantation of engineered nerve graft substitutes has emerged as a promising alternative for peripheral nerve repair.

Nerve tissue comprises highly oriented and densely packed cellular fiber bundles [159]. The Schwann cells (SCs) are arranged in strings along the axons and envelop them, which facilitates the rapid conduction of nerve impulses due to their unique distribution [160, 161]. Consequently, the current research focuses on establishing connections between damaged nerve tissues to facilitate repair. Yao et al. fabricated a microfibrous scaffold with cell-scale spacing (5–20 μm) by MEW. The biomimetic design can significantly promote the cell migration speed and the growth length of neurites (increasing by 40%). This optimized micron-scale fiber arrangement provides a new strategy for the design of neural tissue engineering scaffolds by offering biomimetic ECM topological cues, reducing the mechanical resistance of cell movement, and guiding the directional extension of neurites simultaneously (Fig. 9a) [52].

Furthermore, as neural cells are excitable, their functions are significantly influenced by external electrical stimulation, which serves as a crucial factor in enhancing neural cell differentiation and nerve regeneration [162]. Chen et al. coated a PCL fibrous scaffold with a conductive gold nanolayer, significantly enhancing scaffold's conductivity. The conductive scaffolds showed the potential to promote the formation of the ECM and stimulate neurite growth (Fig. 9b) [86]. In addition, O' Brien et al. fabricated a hybrid scaffold consisting of neurotrophic ECM and PPY coated PCL scaffolds, which can direct axonal regrowth across the injury lesion [163]. Notably, MEW not only provides a versatile platform for fabricating biomimetic scaffolds that support the survival and functional behavior of electroactive nerve cells but also enables new opportunities to study neural network behavior and nerve repair mechanisms in vitro [87, 88].

5 Challenges and Future Perspectives

In this review, we have summarized current design strategies and fabrication processes for producing tissue engineering scaffolds using the MEW technique. Owing to its unique ability to replicate native tissue microarchitecture with high fidelity, MEW has emerged as a valuable biofabrication tool in regenerative medicine. Continued development of MEW now focuses on overcoming application-specific challenges and expanding its functional potential across diverse tissue types.

5.1 Cardiac Tissue Engineering

In cardiac tissue engineering, the design of MEW scaffolds should possess suitable mechanical properties, multilayer aligned structure, and suitable conductivity. However, the designs of MEW scaffolds in recent years have been unable to meet all these requirements simultaneously. In future research, these requirements need to be taken into

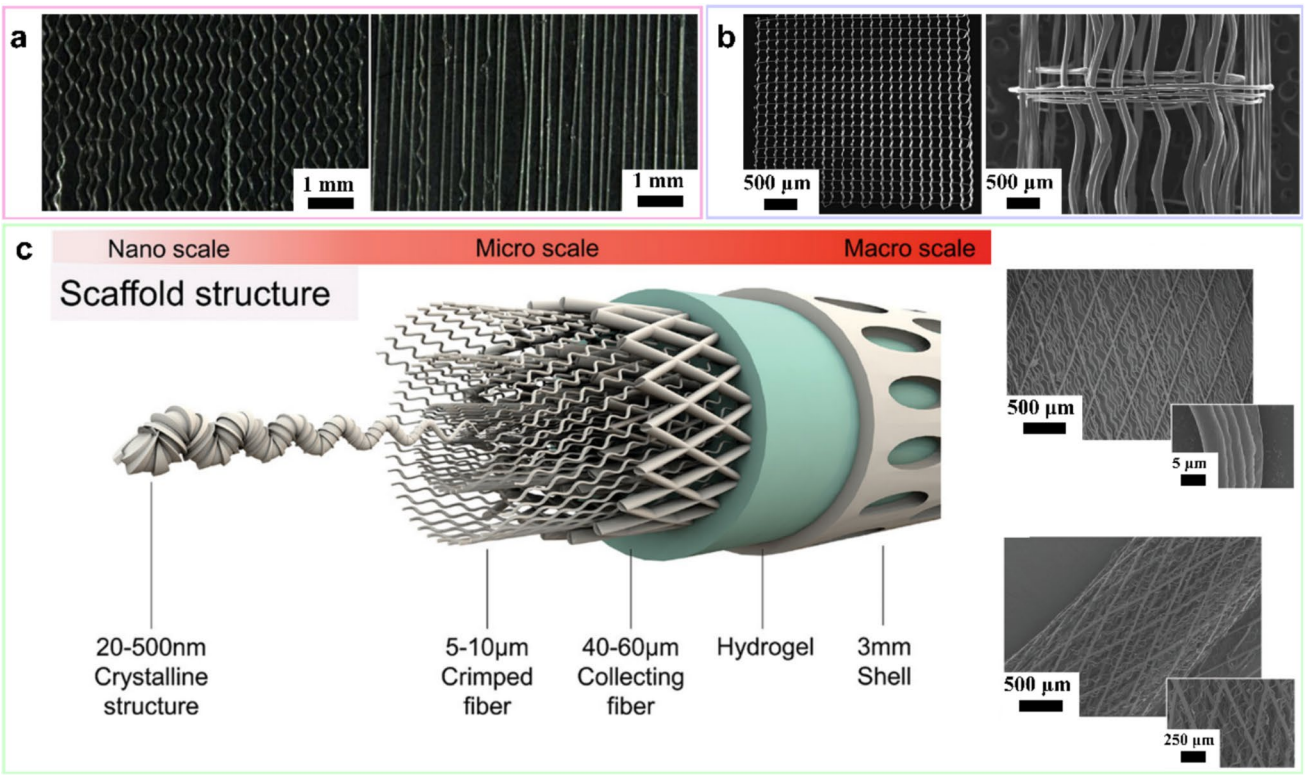

Fig. 7 MEW scaffolds for ligament and tendon tissue engineering. **a** Tensile testing of straight and sinusoidal scaffolds with and without cyclic preloading; Reproduced with permission from Ref. [42], Copyright 2018, Elsevier. **b** Scaffolds with crimped fibers before and after rolling; reproduced with permission from Ref. [149], Copyright 2017, Elsevier. **c** Multiscale structures of biomimetic tendon scaffolds before and after rolling; Reproduced with permission from Ref. [150], Copyright 2024, Wiley–VCH

consideration. For instance, oriented fibers can be printed on the surface of the anisotropic fibrous scaffolds to promote cell orientation and structure-driven processes [164]. While researchers have developed scaffolds with diverse microstructures to enhance deformability, these designs remain limited to two-dimensional deformation. Achieving scaffolds that can accommodate complex, synergistic deformation with the beating heart remains a significant challenge. Furthermore, PCL remains the primary biomaterial used in MEW, but its high stiffness can hinder mechanical signal transmission from beating CMs to the scaffold. Thus, developing new, compliant materials suitable for MEW is a critical direction. In addition, effective strategies for modifying scaffolds with bioactive, conductive materials are needed to replicate the electroactivity of native cardiac tissue. Low cell seeding densities also impair the functional integration of CMs with the scaffold, further limiting synchronous contraction. Thus, future research should focus on the integration of MEW scaffolds with cell-laden hydrogels. Addressing these challenges will be essential for advancing MEW in cardiac applications.

5.2 Bone Regeneration

Future work in bone tissue engineering should focus on designing scaffolds that mimic the hierarchical and anisotropic architecture of native bone, which is crucial for promoting regeneration and vascularization [165]. Moreover, the extensive existing vascular networks can promote nutrient transportation and further enhance bone repair and regeneration. Thus, the integration of vascularization into MEW scaffolds can further enhance the biomimetic function and provide a more efficient regenerative capability for the bone defect area. Another interesting research area is about the formation mechanism of nHA during the bone repair process. Future research can utilize the fibrous scaffold constructed by MEW to study this process. Among them, the incorporation of piezoelectric materials is a promising research topic, as piezoelectric nanoparticles can effectively promote the differentiation, migration, and bone regeneration of osteoblasts [166].

Notably, the clinical translation still remains the current focus of research. Although experiments in vitro

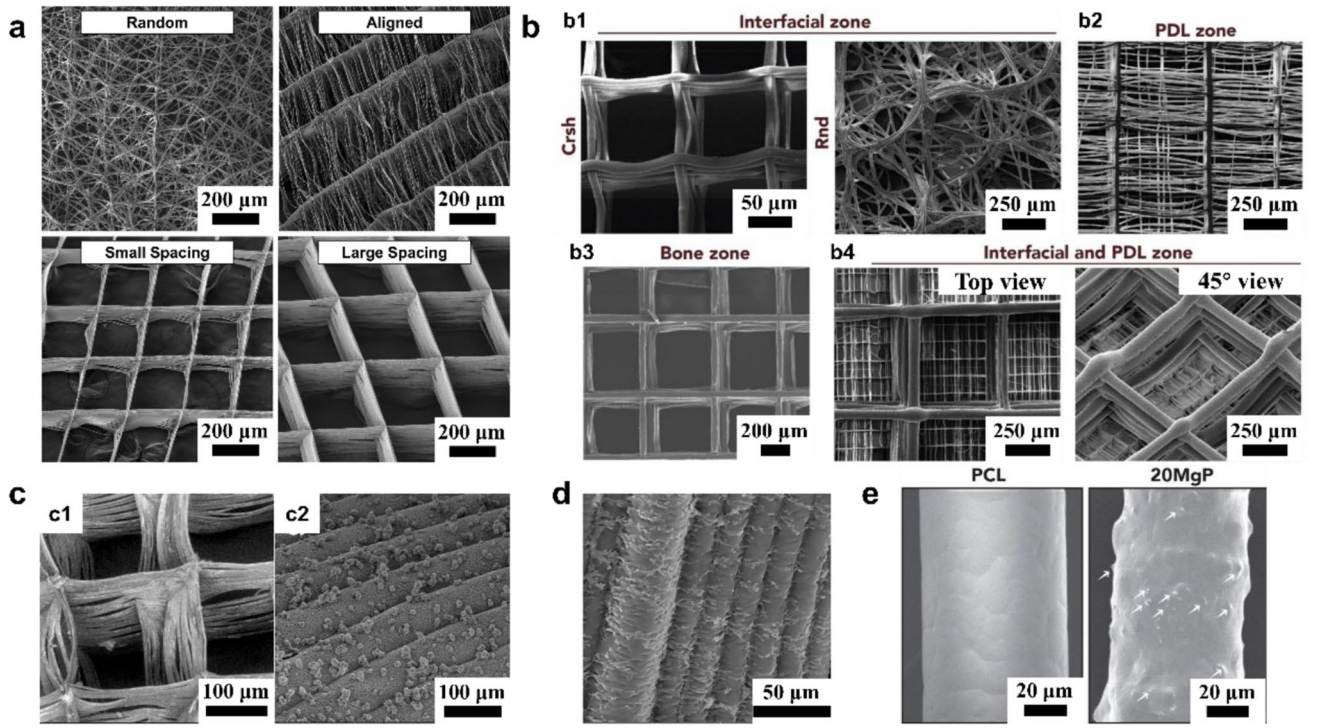

Fig. 8 MEW scaffolds for periodontal regeneration. **a** MEW fibrous scaffolds with distinct fiber configuration and highly ordered architectures; Reproduced with permission from Ref. [83], Copyright 2023, KeAi. **b** MEW scaffolds of the crosshatch random structure, highly aligned PCL fibers for the PDL zone, 20MgP fibers for the bone zone, and interfacial crosshatch and PDL zones from top and side views, respectively; reproduced with permission from Ref. [63], Copyright 2023, American Chemical Society. **c** Surface morphology of PCL scaffolds coated with CaP layer; Reproduced with permission from Ref. [84], Copyright 2023, KeAi. **d** MEW scaffolds after F/CaP coating; reproduced with permission from Ref. [85], Copyright 2021, Wiley–VCH. **e** Single fiber of PCL and 20MgP (MgP particles identified with white arrows); Reproduced with permission from Ref. [63], Copyright 2023, American Chemical Society

can demonstrate the biocompatibility of MEW scaffolds, further research on bone tissue engineering scaffolds still needs to pay attention to the interaction between native tissue and the MEW scaffolds. Specifically, when MEW scaffolds are implanted, they can undergo deformation within the defect and compression from surrounding muscle tissue. MEW scaffolds should mitigate this deformation and support new bone formation.

The investigation of surface topography represents another area for future exploration. Appropriate surface topography cues can enhance hydrophilicity, which profoundly influences the biological interactions between the surrounding environment and biomaterials. This includes the adhesion and adsorption of proteins, cell behavior, and ultimately the process of osteointegration. Furthermore, hydrogels possess excellent drug loading and controlled release capabilities. Therefore, the combination of fibrous scaffolds and hydrogels is a promising candidate material for treating bone defects [167].

5.3 Cartilage Tissue Engineering

Current MEW scaffold designs for cartilage repair mainly focus on mechanical properties and growth factor delivery, with insufficient consideration given to the curved surface structure inherent to native cartilage—a critical feature for load-bearing function [168]. Furthermore, conventional polymeric fibers often yield stiff and non-compliant constructs that fail to mimic the viscoelastic behavior of cartilage, potentially causing damage to adjacent joint tissues. While PCL offers good biocompatibility and printability, its slow degradation rate and limited biological activity restrict its effectiveness. Despite these promising directions, there remains a pressing need for more refined large-animal studies that closely replicate human physiological conditions to validate the translational potential of such innovative scaffold designs.

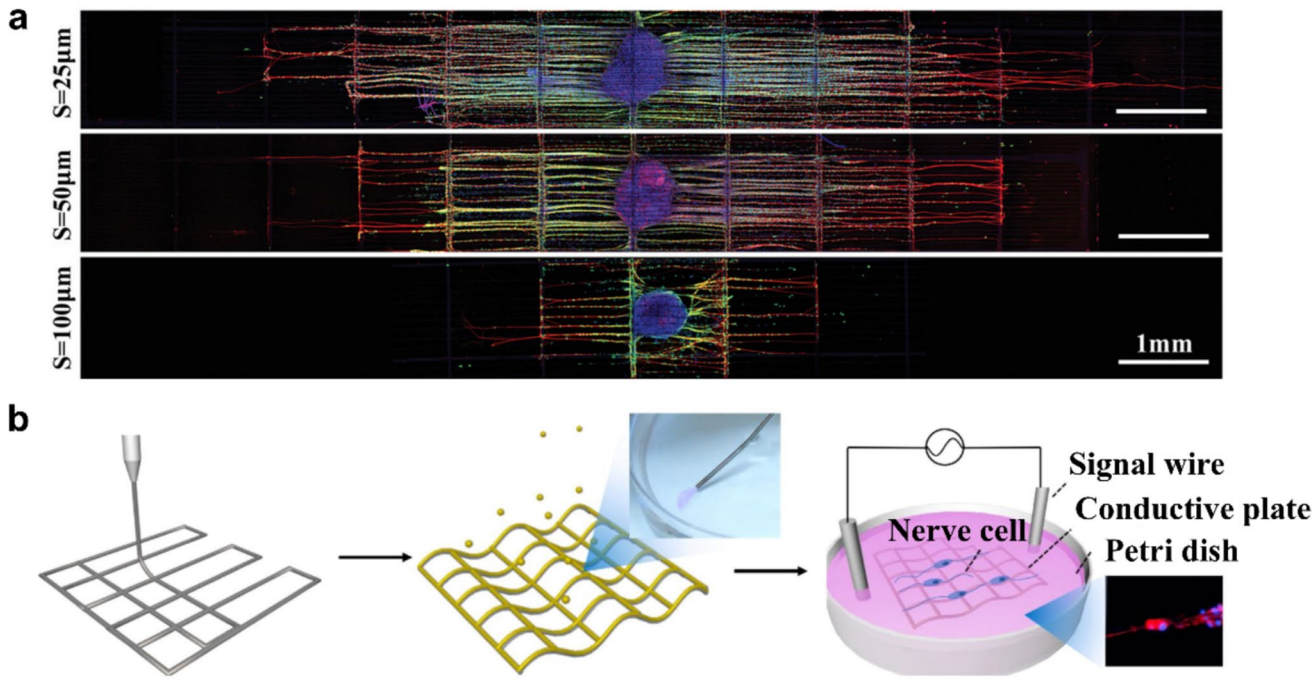

Fig. 9 MEW scaffolds for nerve repair. **a** Morphology of dorsal root ganglions cultured for 7 days on PCL microfibers with different fiber spacings at day 7; reproduced with permission from Ref. [52], Copyright 2023, Wiley–VCH. **b** Schematics of the preparation of injectable Au–PCL scaffolds with high conductivity and high-throughput stimulation device for nerve cells; Reproduced with permission from Ref. [86], Copyright 2020, Elsevier

5.4 Vascular Scaffolds

In vascular tissue engineering, variability in scaffolds design and implantation techniques remains a major challenge. Future efforts should aim to replicate native vascular architecture by incorporating layer-specific, directional, and multi-cellular designs [169]. Moreover, further research is necessary to optimize the reendothelialization of MEW scaffolds to create a smooth and continuous surface akin to a natural lumen. Strategies such as incorporating ECM components can enhance mechanical performance, but ensuring sufficient sealing of scaffolds remains a persistent challenge. In terms of mechanical performance evaluation, simulating pulsating flow mechanical stimulation through dynamic culture is valuable for assessing the performance of the scaffold before conducting in vivo tests for long-term patency.

5.5 Ligament and Tendon Tissue Engineering

MEW has shown unique potential in the fabrication of ligament and tendon scaffolds. However, the clinical translation remains difficult due to the need for hierarchical fibrous structures that replicate both nanoscale and macroscale features, including the complex ligament–bone interface. Further studies may focus on the combination of MEW and electrospinning to construct the multiscale structures [170]. In addition, ligament and tendon regeneration require scaffolds that can mimic the in vivo mechanical loading environment. Static culture conditions are often insufficient to guide the directional differentiation of cells. Integrating 4D printing with stimuli-responsive materials (e.g., pH- or temperature-sensitive polymers) may offer a route to dynamic, biomechanically responsive scaffold systems.

5.6 Periodontal Regeneration

The construction of the ligament-to-bone interface in periodontal tissue is a critical challenge. The challenges of multi-tissue regeneration necessitate careful consideration of tissue structure, cell type, and soft-to-hard tissue interfaces. Another significant concern is the risk of bacterial infection during surgical treatment, which can lead to oral diseases caused by bacteria in the periodontal tissues. Therefore, future studies should explore the incorporation of antibacterial materials into the biomimetic scaffolds to address potential bacterial infections during surgery. Moreover, modifying the wetting properties of the surface of the fibrous scaffold through surface treatment can affect the antibacterial ability of the scaffold [171]. Large animal models

simulating chronic periodontal inflammation are also necessary to evaluate the scaffold performance under clinically relevant conditions.

5.7 Nerve Repair

Although MEW technology has broad application prospects for neural repair, it still faces the following challenges. One challenge is to construct neural structures that are close to native neural structures. The nerve conduit requires an internal hollow structure to guide the growth of axons [172]. Therefore, future research needs to construct a hollow 3D structure using a rotating mandrel collector. Another challenge is the implantation of nerve scaffolds which are difficult to achieve interface and signal connectivity with natural tissues in vivo. Hence, the future research should focus on optimizing the design of neural interfaces to boost the efficiency and precision of signal transmission. Meanwhile, integrating interdisciplinary research findings to drive technological innovation is crucial. Artificial intelligence or machine learning technologies can be incorporated to improve their efficacy and accuracy in neural repair. In addition, it is imperative to strengthen the bridge between basic research and clinical application, ensuring that the latest scientific advancements are swiftly translated into clinical practice.

Moving forward, the advancement of MEW in tissue engineering will rely on the convergence of material science, biofabrication technologies, and systems biology. Rather than solving isolated engineering challenges, future progress will depend on designing integrated, adaptable platforms that respond to biological complexity and therapeutic demands. Collaboration across disciplines—including regenerative biology, data science, and clinical medicine—will be essential to translate MEW from precision manufacturing into functional, patient-specific solutions. In the future, MEW is positioned not just as a fabrication tool, but as a strategic enabler in the development of next-generation regenerative therapies.

Acknowledgements This work was supported by the National Natural Science Foundation of China (Grant Numbers: 12402377, 12272253), the Fundamental Research Program of Shanxi Province, China (Grant Numbers: 202403021223002 202203021212215, 20210302123132). J.C. acknowledges support from the UCL GEF (574696). Furthermore, the authors also acknowledge the use of BioRender.com for creating part of the figures.

Data availability Data availability is not applicable to this article as no new data were created or analyzed in this study.

Declarations

Conflict of interest The authors declare no conflict of interest.

References

1. Ingavle GC, Leach JK. Advancements in electrospinning of polymeric nanofibrous scaffolds for tissue engineering. *Tissue Eng Part B Rev*. **2014**;*20*:277.
2. Lv X, Feng C, Liu Y, Peng X, Chen S, Xiao D, Wang H, Li Z, Xu Y, Lu M. A smart bilayered scaffold supporting keratinocytes and muscle cells in micro/nano-scale for urethral reconstruction. *Theranostics*. **2018**;*8*:3153.
3. Walma DAC, Yamada KM. The extracellular matrix in development. *Development*. **2020**;*147*:dev175596.
4. Zheng D-W, Hong S, Zhang Q-L, Dong X, Pan P, Song W-F, Song W, Cheng S-X, Zhang X-Z. Controllable gelation of artificial extracellular matrix for altering mass transport and improving cancer therapies. *Nat Commun*. **2020**;*11*:4907.
5. Augustine R, Dan P, Hasan A, Khalaf IM, Prasad P, Ghosal K, Gentile C, McClements L, Maureira P. Stem cell-based approaches in cardiac tissue engineering: controlling the microenvironment for autologous cells. *Biomed Pharmacother*. **2021**;*138*: 111425.
6. Burloiu AM, Ozon EA, Musuc AM, Anastasescu M, Socoteanu RP, Atkinson I, Culita DC, Anuta V, Popescu IA, Lupuliasa D, Mihai DP, Gîrd CE, Boscencu R. Porphyrin photosensitizers into polysaccharide-based biopolymer hydrogels for topical photodynamic therapy: physicochemical and pharmacotechnical assessments. *Gels*. **2024**;*10*:499.
7. Bl O, Panneer Selvam S, Ramadoss R, Sundar S, Ramani P, P B. Fabrication of periodontal membrane from *nelumbo nucifera*: a novel approach for dental applications. *Cureus J Med Science*. **2024**;*16*: e59848.
8. Zhang B, Li S, Zhang Z, Meng Z, He J, Ramakrishna S, Zhang C. Intelligent biomaterials for micro and nanoscale 3D printing. *Curr Opin Biomed Eng*. **2023**;*26*: 100454.
9. He J, Zhang B, Li Z, Mao M, Li J, Han K, Li D. High-resolution electrohydrodynamic bioprinting: a new biofabrication strategy for biomimetic micro/nanoscale architectures and living tissue constructs. *Biofabrication*. **2020**;*12*: 042002.
10. Zhang Y-Q, Wang P, Shi Q-F, Ning X, Chen Z, Ramakrishna S, Zheng J, Long Y-Z. Advances in wet electrospinning: rich morphology and promising applications. *Adv Fiber Mater*. **2024**;*7*:374.
11. Li W, Yin Y, Zhou H, Fan Y, Yang Y, Gao Q, Li P, Gao G, Li J. Recent advances in electrospinning techniques for precise medicine. *Cyborg Bionic Syst*. **2024**;*5*:0101.
12. Zhao Y, Zhang Z, Pan Z, Liu Y. Advanced bioactive nanomaterials for biomedical applications. *Exploration*. **2021**;*1*:20210089.
13. Almubarak S, Nethercott H, Freeberg M, Beaudon C, Jha A, Jackson W, Marcucio R, Miclau T, Healy K, Bahney C. Tissue engineering strategies for promoting vascularized bone regeneration. *Bone*. **2016**;*83*:197.

14. Ji Y, Yang Q, Huang G, Shen M, Jian Z, Thoraval M-J, Lian Q, Zhang X, Xu F. Improved resolution and fidelity of droplet-based bioprinting by upward ejection. *ACS Biomater Sci Eng*. **2019**;*5*:4112.
15. Nazir A, Ali M, Jeng J-Y. Investigation of compression and buckling properties of a novel surface-based lattice structure manufactured using multi jet fusion technology. *Materials*. **2021**;*14*:2599.
16. Pennacchio FA, Caliendo F, Iaccarino G, Langella A, Siciliano V, Santoro F. Three-dimensionally patterned scaffolds modulate the biointerface at the nanoscale. *Nano Lett*. **2019**;*19*:5118.
17. Teixeira BN, Aprile P, Mendonca RH, Kelly DJ, Thire R. Evaluation of bone marrow stem cell response to PLA scaffolds manufactured by 3D printing and coated with polydopamine and type I collagen. *J Biomed Mater Res B Appl Biomater*. **2019**;*107*:37.
18. Saiz PG, Reizabal A, Vilas-Vilela JL, Dalton PD, Lanceros-Mendez S. Materials and strategies to enhance melt electrowriting potential. *Adv Mater*. **2024**;*36*: 2312084.
19. Yang R, Xu Y, Li R, Zhang Y, Xu Y, Yang L, Cui W, Wang L. Synergistic biofilter tube for promoting scarless tendon regeneration. *Nano Lett*. **2024**;*24*:7381.
20. Wan X, Zhao Y, Li Z, Li L. Emerging polymeric electrospun fibers: from structural diversity to application in flexible bioelectronics and tissue engineering. *Exploration*. **2022**;*2*:20210029.
21. Loewner S, Heene S, Baroth T, Heymann H, Cholewa F, Blume H, Blume C. Recent advances in melt electro writing for tissue engineering for 3D printing of microporous scaffolds for tissue engineering. *Front Bioeng Biotechnol*. **2022**;*10*: 896719.
22. Zhou X, Fang Y, Zhang T, Xiong Z. Retrospective: advances and opportunities of 3D bioprinting in China over three decades. *Addit Manuf Front*. **2024**;*3*: 200157.
23. Salem M, Khadivi F, Javanbakht P, Mojaverrostami S, Abbasi M, Feizollahi N, Abbasi Y, Heidarian E, Rezaei YF. Advances of three-dimensional (3D) culture systems for in vitro spermatogenesis. *Stem Cell Res Ther*. **2023**;*14*:262.
24. Luo G, Teh KS, Liu Y, Zang X, Wen Z, Lin L. Direct-write, self-aligned electrospinning on paper for controllable fabrication of three-dimensional structures. *ACS Appl Mater Interfaces*. **2015**;*7*:27765.
25. Wu Y. Electrohydrodynamic jet 3D printing in biomedical applications. *Acta Biomater*. **2021**;*128*: 21.
26. Liu Z, Jia J, Lei Q, Wei Y, Hu Y, Lian X, Zhao L, Xie X, Bai H, He X, Si L, Livermore C, Kuang R, Zhang Y, Wang J, Yu Z, Ma X, Huang D. Electrohydrodynamic direct-writing micro/nanofibrous architectures: principle, materials, and biomedical applications. *Adv Healthc Mater*. **2024**;*13*: 2400930.
27. Hrynevich A, Elçi BŞ, Haigh JN, McMaster R, Youssef A, Blum C, Blunk T, Hochleitner G, Groll J, Dalton PD. Dimension-based design of melt electrowritten scaffolds. *Small*. **2018**;*14*:1800232.
28. Eichholz KF, Gonçalves I, Barceló X, Federici AS, Hoey DA, Kelly DJ. How to design, develop and build a fully-integrated melt electrowriting 3D printer. *Addit Manuf*. **2022**;*58*: 102998.
29. Kade JC, Dalton PD. Polymers for melt electrowriting. *Adv Healthc Mater*. **2020**;*10*: 2001232.
30. Mieszczanek P, Robinson TM, Dalton PD, Hutmacher DW. Convergence of machine vision and melt electrowriting. *Adv Mater*. **2021**;*33*: 2100519.
31. Ding H, Cao K, Zhang F, Boettcher W, Chang RC. A fundamental study of charge effects on melt electrowritten polymer fibers. *Mater Des*. **2019**;*178*: 107857.
32. Montero-Calle P, Flandes-Iparraguirre M, Mountris K, de la S Nava A, Laita N, Rosales RM, Iglesias-García O, de-Juan-Pardo EM, Atienza F, Fernández-Santos ME, Peña E, Doblaré M, Gavira JJ, Fernández-Avilés F, Prósper F, Pueyo E, Mazo MM. Fabrication of human myocardium using multidimensional modelling of engineered tissues. *Biofabrication*. **2022**;*14*: 045017.
33. Tourlomousis F, Ding H, Kalyon DM, Chang RC. Melt electrospinning writing process guided by a "printability number." *J Manuf Sci Eng*. **2017**;*139*: 081004.
34. McColl E, Groll J, Jungst T, Dalton PD. Design and fabrication of melt electrowritten tubes using intuitive software. *Mater Des*. **2018**;*155*: 46.
35. Dayan CB, Afghah F, Okan BS, Yıldız M, Menceloglu Y, Culha M, Koc B. Modeling 3D melt electrospinning writing by response surface methodology. *Mater Des*. **2018**;*148*: 87.
36. Du L, Nie L, Zhang L, Lu H, Yang L, Xu H, Hou J. Enhancing the printing accuracy of melt electrowritten fibers deposited on aluminum foils. *Mater Lett*. **2022**;*321*: 132397.
37. Lu H, Sun Y, Chen Y, Nie L, Yang L, Du L, Xu H. The effects of voltage configurations on print accuracy in melt electrowriting. *Mater Lett*. **2023**;*334*: 133738.
38. Hochleitner G, Jüngst T, Brown TD, Hahn K, Moseke C, Jakob F, Dalton PD, Groll J. Additive manufacturing of scaffolds with sub-micron filaments via melt electrospinning writing. *Biofabrication*. **2015**;*7*: 035002.
39. Wunner FM, Wille ML, Noonan TG, Bas O, Dalton PD, De-Juan-Pardo EM, Hutmacher DW. Melt electrospinning writing of highly ordered large volume scaffold architectures. *Adv Mater*. **2018**;*30*: 1706570.
40. King W, Bowlin G. Near-field electrospinning and melt electrowriting of biomedical polymers—progress and limitations. *Polymers*. **2021**;*13*: 1097.
41. Wang Y, Su Y, Zhang Y, Chen M. High-voltage wave induced a unique structured percolation network with a negative gauge factor. *ACS Appl Mater Interfaces*. **2022**;*14*:5661.
42. Hochleitner G, Chen F, Blum C, Dalton PD, Amsden B, Groll J. Melt electrowriting below the critical translation speed to fabricate crimped elastomer scaffolds with non-linear extension behaviour mimicking that of ligaments and tendons. *Acta Biomater*. **2018**;*72*: 110.
43. Lei Q, Jia J, Guan X, Han K, Liu J, Duan R, Lian X, Huang D. Electrohydrodynamic printing of microscale fibrous scaffolds with a sinusoidal structure for enhancing the contractility of cardiomyocytes. *ACS Biomater Sci Eng*. **2024**;*10*:7227.
44. Han K, Mao M, Fu L, Zhang Y, Kang Y, Li D, He J. Multimaterial printing of serpentine microarchitectures with synergistic mechanical/piezoelectric stimulation for enhanced cardiac-specific functional regeneration. *Small*. **2024**;*20*:2401561.
45. Peiffer QC, de Ruijter M, van Duijn J, Crottet D, Dominic E, Malda J, Castilho M. Melt electrowriting onto anatomically relevant biodegradable substrates: resurfacing a diarthrodial joint. *Mater Des*. **2020**;*195*: 109025.
46. Weekes A, Wehr G, Pinto N, Jenkins J, Li Z, Meinert C, Klein TJ. Highly compliant biomimetic scaffolds for small diameter tissue-engineered vascular grafts (TEVGs) produced via melt electrowriting (MEW). *Biofabrication*. **2023**;*16*: 015017.
47. Saidy NT, Fernández-Colino A, Heidari BS, Kent R, Vernon M, Bas O, Mulderrig S, Lubig A, Rodríguez-Cabello JC, Doyle B, Hutmacher DW, De-Juan-Pardo EM, Mela P. Spatially heterogeneous tubular scaffolds for In situ heart valve tissue engineering using melt electrowriting. *Adv Funct Mater*. **2022**;*32*: 2110716.
48. McCosker AB, Snowdon ME, Lamont R, Woodruff MA, Paxton NC. Exploiting nonlinear fiber patterning to control tubular scaffold mechanical behavior. *Adv Mater Technol*. **2022**;*7*: 2200259.
49. Cao K, Zhang F, Zaeri A, Zgeib R, Chang RC. A holistic model for melt electrowritten threedimensional structured materials based on residual charge. *Int J Bioprint*. **2022**;*9*: 656.

50. Zhang F, Cao K, Zaeri A, Zgeib R, Chang RC. Effects of printing sequence on the printing accuracy of melt electrowriting scaffolds. *Macromol Mater Eng*. **2022**;*9*: 2200222.
51. Zhang F, Cao K, Zaeri A, Zgeib R, Chang RC. Effects of scaffold design parameters on the printing accuracy for melt electrowriting. *J Manuf Process*. **2022**;*81*:177.
52. Yao C, Qiu Z, Li X, Zhu H, Li D, He J. Electrohydrodynamic printing of microfibrous architectures with cell-scale spacing for improved cellular migration and neurite outgrowth. *Small*. **2023**;*19*:2207331.
53. Liashenko I, Hrynevich A, Dalton PD. Designing outside the box: unlocking the geometric freedom of melt electrowriting using microscale layer shifting. *Adv Mater*. **2020**;*32*: 2001874.
54. Xu H, Liashenko I, Lucchetti A, Du L, Dong Y, Zhao D, Meng J, Yamane H, Dalton PD. Designing with circular arc toolpaths to increase the complexity of melt electrowriting. *Adv Mater Technol*. **2022**;*7*: 2101676.
55. Javadzadeh M, del Barrio J, Sánchez-Somolinos C. Melt electrowriting of liquid crystal elastomer scaffolds with programmed mechanical response. *Adv Mater*. **2023**;*35*: 2209244.
56. Devlin BL, Allenby MC, Ren J, Pickering E, Klein TJ, Paxton NC, Woodruff MA. Materials design innovations in optimizing cellular behavior on melt electrowritten (MEW) scaffolds. *Adv Funct Mater*. **2024**;*34*: 2313092.
57. Böhm C, Stahlhut P, Weichhold J, Hrynevich A, Teßmar J, Dalton PD. The multiweek thermal stability of medical-grade poly(ε-caprolactone) during melt electrowriting. *Small*. **2021**;*18*: 2104193.
58. Paxton NC, Ho SWK, Tuten BT, Lipton-Duffin J, Woodruff MA. Degradation of melt electrowritten PCL scaffolds following melt processing and plasma surface treatment. *Macromol Rapid Commun*. **2021**;*42*:2100433.
59. Kim J, Kim W, Kim G. Scaffold with micro/nanoscale topographical cues fabricated using E-field-assisted 3D printing combined with plasma-etching for enhancing myoblast alignment and differentiation. *Appl Surf Sci*. **2020**;*509*: 145404.
60. Olvera D, Sohrabi Molina M, Hendy G, Monaghan MG. Electroconductive melt electrowritten patches matching the mechanical anisotropy of human myocardium. *Adv Funct Mater*. **2020**;*30*: 1909880.
61. Qu X, Xia P, He J, Li D. Microscale electrohydrodynamic printing of biomimetic PCL/nHA composite scaffolds for bone tissue engineering. *Mater Lett*. **2016**;*185*:554.
62. Bai J, Wang H, Gao W, Liang F, Wang Z, Zhou Y, Lan X, Chen X, Cai N, Huang W, Tang Y. Melt electrohydrodynamic 3D printed poly (ε-caprolactone)/polyethylene glycol/roxithromycin scaffold as a potential anti-infective implant in bone repair. *Int J Pharm*. **2020**;*576*: 118941.
63. Golafshan N, Castilho M, Daghrery A, Alehosseini M, van de Kemp T, Krikonis K, de Ruijter M, Dal-Fabbro R, Dolatshahi-Pirouz A, Bhaduri SB, Bottino MC, Malda J. Composite graded melt electrowritten scaffolds for regeneration of the periodontal ligament-to-bone interface. *ACS Appl Mater Interfaces*. **2023**;*15*: 12735.
64. Qiao Z, Lian M, Han Y, Sun B, Zhang X, Jiang W, Li H, Hao Y, Dai K. Bioinspired stratified electrowritten fiber-reinforced hydrogel constructs with layer-specific induction capacity for functional osteochondral regeneration. *Biomaterials*. **2021**;*266*: 120385.
65. Zhang G, Li W, Yu M, Huang H, Wang Y, Han Z, Shi K, Ma L, Yu Z, Zhu X, Peng Z, Xu Y, Li X, Hu S, He J, Li D, Xi Y, Lan H, Xu L, Tang M, Xiao M. Electric-field-driven printed 3D highly ordered microstructure with cell feature size promotes the maturation of engineered cardiac tissues. *Adv Sci*. **2023**;*10*: 2206264.
66. Meng J, Boschetto F, Yagi S, Marin E, Adachi T, Chen X, Pezzotti G, Sakurai S, Yamane H, Xu H. Melt-electrowritten poly(L-lactic acid)- and bioglass-reinforced biomimetic hydrogel for bone regeneration. *Mater Des*. **2022**;*219*: 110781.
67. Fortelny I, Ujcic A, Fambri L, Slouf M. Phase structure, compatibility, and toughness of PLA/PCL blends: a review. *Front Mater*. **2019**;*6*: 481142.
68. Wang W, Zhang B, Li M, Li J, Zhang C, Han Y, Wang L, Wang K, Zhou C, Liu L, Fan Y, Zhang X. 3D printing of PLA/n-HA composite scaffolds with customized mechanical properties and biological functions for bone tissue engineering. *Compos Part B-Eng*. **2021**;*224*: 109192.
69. Zhang Y, Le Friec A, Sun D, Chen M. Sinusoidal stretchable fibrous electrodes regulate cardiac contraction. *Chem Eng J*. **2023**;*455*: 140555.
70. Castilho M, van Mil A, Maher M, Metz CHG, Hochleitner G, Groll J, Doevendans PA, Ito K, Sluijter JPG, Malda J. Melt electrowriting allows tailored microstructural and mechanical design of scaffolds to advance functional human myocardial tissue formation. *Adv Funct Mater*. **2018**;*28*: 1803151.
71. Eichholz KF, Freeman FE, Pitacco P, Nulty J, Ahern D, Burdis R, Browe DC, Garcia O, Hoey DA, Kelly DJ. Scaffold microarchitecture regulates angiogenesis and the regeneration of large bone defects. *Biofabrication*. **2022**;*14*: 045013.
72. Lei Q, He J, Li D. Electrohydrodynamic 3D printing of layer-specifically oriented, multiscale conductive scaffolds for cardiac tissue engineering. *Nanoscale*. **2019**;*11*:15195.
73. Abbasi N, Abdal-hay A, Hamlet S, Graham E, Ivanovski S. Effects of gradient and offset architectures on the mechanical and biological properties of 3-D melt electrowritten (MEW) scaffolds. *ACS Biomater Sci Eng*. **2019**;*5*:3448.
74. Ainsworth MJ, Lotz O, Gilmour A, Zhang A, Chen MJ, McKenzie DR, Bilek MMM, Malda J, Akhavan B, Castilho M. Covalent protein immobilization on 3D-printed microfiber meshes for guided cartilage regeneration. *Adv Funct Mater*. **2022**;*33*: 2206583.
75. Brennan CM, Eichholz KF, Hoey DA. The effect of pore size within fibrous scaffolds fabricated using melt electrowriting on human bone marrow stem cell osteogenesis. *Biomed Mater*. **2019**;*14*: 065016.
76. Dufour A, Gallostra X B XB, O'Keeffe C, Eichholz K, Von Euw S, Garcia O, Kelly DJ. Integrating melt electrowriting and inkjet bioprinting for engineering structurally organized articular cartilage. *Biomaterials*. **2022**;*283*: 121405.
77. Hall GN, Chandrakar A, Pastore A, Ioannidis K, Moisley K, Cirstea M, Geris L, Moroni L, Luyten FP, Wieringa P, Papantoniou I. Engineering bone-forming biohybrid sheets through the integration of melt electrowritten membranes and cartilaginous microspheroids. *Acta Biomater*. **2023**;*165*:111.
78. Han Y, Lian M, Sun B, Jia B, Wu Q, Qiao Z, Dai K. Preparation of high precision multilayer scaffolds based on melt electrowriting to repair cartilage injury. *Theranostics*. **2020**;*10*:10214.
79. Galarraga JH, Locke RC, Witherel CE, Stoeckl BD, Castilho M, Mauck RL, Malda J, Levato R, Burdick JA. Fabrication of MSC-laden composites of hyaluronic acid hydrogels reinforced with MEW scaffolds for cartilage repair. *Biofabrication*. **2021**;*14*: 014106.
80. Staples R, Ivanovski S, Vaquette C. Fibre-guiding biphasic scaffold for perpendicular periodontal ligament attachment. *Acta Biomater*. **2022**;*150*:221.
81. Mueller KMA, Unterrainer A, Rojas-González DM, De-Juan-Pardo E, Willner MS, Herzen J, Mela P. Introducing controlled microporosity in melt electrowriting. *Adv Mater Technol*. **2023**;*8*: 2201158.

82. Gwiazda M, Kumar S, Świeszkowski W, Ivanovski S, Vaquette C. The effect of melt electrospun writing fiber orientation onto cellular organization and mechanical properties for application in anterior cruciate ligament tissue engineering. *J Mech Behav Biomed Mater*. **2020**;*104*: 103631.
83. Daghrery A, Ferreira JA, Xu J, Golafshan N, Kaigler D, Bhaduri SB, Malda J, Castilho M, Bottino MC. Tissue-specific melt electrowritten polymeric scaffolds for coordinated regeneration of soft and hard periodontal tissues. *Bioact Mater*. **2023**;*19*:268.
84. Farag A, Abdal-hay A, Han P, Ivanovski S. Fabrication of 3D melt electrowritting multiphasic scaffold with bioactive and osteoconductivite functionalities for periodontal regeneration. *Ceram Int*. **2023**;*49*:8015.
85. Daghrery A, Ferreira JA, de Souza Araújo IJ, Clarkson BH, Eckert GJ, Bhaduri SB, Malda J, Bottino MC. A highly ordered, nanostructured fluorinated CaP-coated melt electrowritten scaffold for periodontal tissue regeneration. *Adv Healthc Mater*. **2021**;*10*: 2101152.
86. Wang Y, Zhang Y, Zhang Z, Su Y, Wang Z, Dong M, Chen M. An injectable high-conductive bimaterial scaffold for neural stimulation. *Colloids Surf B Biointerfaces*. **2020**;*195*: 111210.
87. Janzen D, Bakirci E, Wieland A, Martin C, Dalton PD, Villmann C. Cortical neurons form a functional neuronal network in a 3D printed reinforced matrix. *Adv Healthc Mater*. **2020**;*9*: 1901630.
88. Schaefer N, Janzen D, Bakirci E, Hrynevich A, Dalton PD, Villmann C. 3D electrophysiological measurements on cells embedded within fiber-reinforced matrigel. *Adv Healthc Mater*. **2019**;*8*: 1801226.
89. Iglesias-García O, Flandes-Iparraguirre M, Montero-Calle P, Rosales RM, Ullate-Agote A, Sánchez-Bueno A, Larequi E, Anaut-Lusar I, Laita N, Oliván-Viguera A, Iglesias E, Abizanda G, San Martín-Úriz P, Aguirre-Ruiz P, Aranguren XL, de García Yébenes M, Gavira JJ, Martínez MÁ, Peña E, Doblaré M, de-Juan-Pardo EM, Pueyo E, Prosper F, Mazo Vega MM. Biologically-inspired melt electrowriting for the generation of highly biomimetic functional myocardium. *Adv Funct Mater*. **2025**;*35*: 2420106.
90. Qiu Z, Meng Z, Kasimu A, Wang Z, He P, Wang L, Zhao R, Mao M, Tian Y, Kong L, Li D, He J. Consecutive hybrid bioprinting of microfiber-reinforced living muscle constructs with highly-aligned cellular organizations. *Adv Mater*. **2025**;*47*:e10222.
91. Castilho M, Feyen D, Flandes-Iparraguirre M, Hochleitner G, Groll J, Doevendans PAF, Vermonden T, Ito K, Sluijter JPG, Malda J. Melt electrospinning writing of poly-hydroxymethylglycolide-co-ε-caprolactone-based scaffolds for cardiac tissue engineering. *Adv Healthc Mater*. **2017**;*6*: 1700311.
92. Borrelli MA, Turnquist HR, Little SR. Biologics and their delivery systems: trends in myocardial infarction. *Adv Drug Deliv Rev*. **2021**;*173*:181.
93. Karppinen S-M, Heljasvaara R, Gullberg D, Tasanen K, Pihlajaniemi T. Toward understanding scarless skin wound healing and pathological scarring. *F1000Res*. **2019**;*8*: 787.
94. Wu K, Wang Y, Liu R, Wang H, Rui T. The role of mammalian sirtuin 6 in cardiovascular diseases and diabetes mellitus. *Front Physiol*. **2023**;*14*: 1207133.
95. Holfeld J, Nägele F, Pölzl L, Engler C, Graber M, Hirsch J, Schmidt S, Mayr A, Troger F, Pamminger M, Theurl M, Schreinlechner M, Sappler N, Ruttmann-Ulmer E, Schaden W, Cooke JP, Ulmer H, Bauer A, Gollmann-Tepeköylü C, Grimm M. Cardiac shockwave therapy in addition to coronary bypass surgery improves myocardial function in ischaemic heart failure: the CAST-HF trial. *Eur Heart J*. **2024**;*45*:2634.
96. Amezcua R, Shirolkar A, Fraze C, Stout D. Nanomaterials for cardiac myocyte tissue engineering. *Nanomaterials*. **2016**;*6*:133.
97. Deshmukh RS, Kovács KA, Dinnyés A. Drug discovery models and toxicity testing using embryonic and induced pluripotent stem-cell-derived cardiac and neuronal cells. *Stem Cells Int*. **2012**;*2012*: 379569.
98. Tandon B, Magaz A, Balint R, Blaker JJ, Cartmell SH. Electroactive biomaterials: vehicles for controlled delivery of therapeutic agents for drug delivery and tissue regeneration. *Adv Drug Deliv Rev*. **2018**;*129*:148.
99. Hosoyama K, Ahumada M, McTiernan CD, Davis DR, Variola F, Ruel M, Liang W, Suuronen EJ, Alarcon EI. Nanoengineered electroconductive collagen-based cardiac patch for infarcted myocardium repair. *ACS Appl Mater Interfaces*. **2018**;*10*:44668.
100. You J-O, Rafat M, Ye GJC, Auguste DT. Nanoengineering the heart: conductive scaffolds enhance connexin 43 expression. *Nano Lett*. **2011**;*11*:3643.
101. Chen Q-Z, Harding SE, Ali NN, Lyon AR, Boccaccini AR. Biomaterials in cardiac tissue engineering: ten years of research survey. *Mater Sci Eng R Rep*. **2008**;*59*: 1.
102. Ramadan S, Paul N, Naguib HE. Standardized static and dynamic evaluation of myocardial tissue properties. *Biomed Mater*. **2017**;*12*: 025013.
103. Kapnisi M, Mansfield C, Marijon C, Guex AG, Perbellini F, Bardi I, Humphrey EJ, Puetzer JL, Mawad D, Koutsogeorgis DC, Stuckey DJ, Terracciano CM, Harding SE, Stevens MM. Auxetic cardiac patches with tunable mechanical and conductive properties toward treating myocardial infarction. *Adv Funct Mater*. **2018**;*28*: 1800618.
104. Li Y, Wei L, Lan L, Gao Y, Zhang Q, Dawit H, Mao J, Guo L, Shen L, Wang L. Conductive biomaterials for cardiac repair: a review. *Acta Biomater*. **2022**;*139*:157.
105. Yong KW, Choi JR, Choi JY, Cowie AC. Recent advances in mechanically loaded human mesenchymal stem cells for bone tissue engineering. *Int J Mol Sci*. **2020**;*21*:5816.
106. Lee S-H, Kim C-H, Yoon J-Y, Choi E-J, Kim MK, Yoon J-U, Kim HY, Kim E-J. Lidocaine intensifies the anti-osteogenic effect on inflammation-induced human dental pulp stem cells via mitogen-activated protein kinase inhibition. *J Dent Sci*. **2023**;*18*:1062.
107. Zhan J, Chen Z, Liu J, Pang Q, Lei M, Liu J, Song Y, Huang W, Dong L. A targeting trained immunity nanofiber scaffold for large bone defect repair. *Adv Fiber Mater*. **2025**;*7*:1423.
108. Wang M, Li B, Liu Y, Tang L, Zhang Y, Xie Q. A novel bionic extracellular matrix polymer scaffold enhanced by calcium silicate for bone tissue engineering. *ACS Omega*. **2021**;*6*:35727.
109. Xiao L, Liu H, Wu S, Huang H, Xie Y, Wei R, Lei J, Lei Y, Xue L, Yan F, Geng Z, Cai L. Fishnet-inspired 3D scaffold fabricated from mesh-like electrospun membranes promoted osteoporotic bone regeneration. *Adv Fiber Mater*. **2024**;*7*:72.
110. Scocozza F, Di Gravina GM, Bari E, Auricchio F, Torre ML, Conti M. Prediction of the mechanical response of a 3D (bio) printed hybrid scaffold for improving bone tissue regeneration by structural finite element analysis. *J Mech Behav Biomed Mater*. **2023**;*142*: 105822.
111. De Witte TM, Wagner AM, Fratila-Apachitei LE, Zadpoor AA, Peppas NA. Immobilization of nanocarriers within a porous chitosan scaffold for the sustained delivery of growth factors in bone tissue engineering applications. *J Biomed Mater Res*. **2020**;*108*:1122.
112. Dong C, Lv Y. Application of collagen scaffold in tissue engineering: recent advances and new perspectives. *Polymers*. **2016**;*8*: 42.
113. Park D, Lee SJ, Choi DK, Park J-W. Therapeutic agent-loaded fibrous scaffolds for biomedical applications. *Pharmaceutics*. **2023**;*15*:1522.
114. Beheshtizadeh N, Azami M, Abbasi H, Farzin A. Applying extrusion-based 3D printing technique accelerates fabricating complex biphasic calcium phosphate-based scaffolds for bone tissue regeneration. *J Adv Res*. **2022**;*40*:69.

115. Bohner M, Miron RJ. A proposed mechanism for material-induced heterotopic ossification. *Mater Today*. **2019**;*22*:132.
116. Freeman FE, Pitacco P, Dommelen LHAv, Nulty J, Browe DC, Shin J-Y, Alsberg E, Kelly DJ. 3D bioprinting spatiotemporally defined patterns of growth factors to tightly control tissue regeneration. *Sci Adv*. **2020**;*6*: eabb5093.
117. Berner A, Woodruff MA, Lam CXF, Arafat MT, Saifzadeh S, Steck R, Ren J, Nerlich M, Ekaputra AK, Gibson I, Hutmacher DW. Effects of scaffold architecture on cranial bone healing. *Int J Oral Maxillofac Surg*. **2014**;*43*:506.
118. Chocholata P, Kulda V, Babuska V. Fabrication of scaffolds for bone-tissue regeneration. *Materials*. **2019**;*12*: 568.
119. Yilgor P, Yilmaz G, Onal MB, Solmaz I, Gundogdu S, Keskil S, Sousa RA, Reis RL, Hasirci N, Hasirci V. Anin vivostudy on the effect of scaffold geometry and growth factor release on the healing of bone defects. *J Tissue Eng Regen Med*. **2013**;*7*:687.
120. O'Brien FJ, Harley BA, Yannas IV, Gibson LJ. The effect of pore size on cell adhesion in collagen-GAG scaffolds. *Biomaterials*. **2005**;*26*:433.
121. Zhang K, Fan Y, Dunne N, Li X. Effect of microporosity on scaffolds for bone tissue engineering. *Regen Biomater*. **2018**;*5*:115.
122. Murphy CM, O'Brien FJ. Understanding the effect of mean pore size on cell activity in collagen-glycosaminoglycan scaffolds. *Cell Adhes Migr*. **2014**;*4*:377.
123. Meng J, Boschetto F, Yagi S, Marin E, Adachi T, Chen X, Pezzotti G, Sakurai S, Sasaki S, Aoki T, Yamane H, Xu H. Enhancing the bioactivity of melt electrowritten PLLA scaffold by convenient, green, and effective hydrophilic surface modification. *Biomater Adv*. **2022**;*135*: 112686.
124. Reznikov N, Bilton M, Lari L, Stevens MM, Kröger R. Fractal-like hierarchical organization of bone begins at the nanoscale. *Science*. **2018**;*360*: eaao2189.
125. Zeng M, Xu Z, Song Z-Q, Li J-X, Tang Z-W, Xiao S, Wen J. Diagnosis and treatment of chronic osteomyelitis based on nanomaterials. *World J Orthop*. **2023**;*14*:42.
126. Eichholz KF, Von Euw S, Burdis R, Kelly DJ, Hoey DA. Development of a new bone-mimetic surface treatment platform: nanoneedle hydroxyapatite (nnHA) coating. *Adv Healthc Mater*. **2020**;*9*: 2001102.
127. Li Y, Ma J, Wang J, Kong Y, Wang F, Zhang P, Yawei F. Optimal parameter setting and evaluation for ultraviolet-assisted direct ink writing bioprinting of nHA/PEGDA scaffold. *Biomed Mater*. **2024**;*20*: 015032.
128. Afghah F, Iyison NB, Nadernezhad A, Midi A, Sen O, Saner Okan B, Culha M, Koc B. 3D fiber reinforced hydrogel scaffolds by melt electrowriting and gel casting as a hybrid design for wound healing. *Adv Healthc Mater*. **2022**;*11*: 2102068.
129. Fang X-Z, Zhou T, Xu J-Q, Wang Y-X, Sun M-M, He Y-J, Pan S-W, Xiong W, Peng Z-K, Gao X-H, Shang Y. Structure, kinetic properties and biological function of mechanosensitive piezo channels. *Cell Biosci*. **2021**;*11*:13.
130. Chen C, Tambe DT, Deng L, Yang L. Biomechanical properties and mechanobiology of the articular chondrocyte. *Am J Physiol Cell Physiol*. **2013**;*305*:C1202.
131. Nordberg RC, Bielajew BJ, Takahashi T, Dai S, Hu JC, Athanasiou KA. Recent advancements in cartilage tissue engineering innovation and translation. *Nat Rev Rheumatol*. **2024**;*20*:323.
132. Lafuente-Merchan M, Ruiz-Alonso S, García-Villén F, Gallego I, Gálvez-Martín P, Saenz-del-Burgo L, Pedraz JL. Progress in 3D bioprinting technology for osteochondral regeneration. *Pharmaceutics*. **2022**;*14*:1578.
133. Steele JAM, Moore AC, St-Pierre J-P, McCullen SD, Gormley AJ, Horgan CC, Black CRM, Meinert C, Klein T, Saifzadeh S, Steck R, Ren J, Woodruff MA, Stevens MM. In vitro and in vivo investigation of a zonal microstructured scaffold for osteochondral defect repair. *Biomaterials*. **2022**;*286*: 121548.
134. Guo T, Lembong J, Zhang LG, Fisher JP. Three-dimensional printing articular cartilage: recapitulating the complexity of native tissue. *Tissue Eng Part B-Re*. **2017**;*23*:225.
135. Kang Y, Guan Y, Li S. Innovative hydrogel solutions for articular cartilage regeneration: a comprehensive review. *Int J Surg*. **2024**;*110*:7984.
136. Su X, Wei L, Xu Z, Qin L, Yang J, Zou Y, Zhao C, Chen L, Hu N. Evaluation and application of silk fibroin based biomaterials to promote cartilage regeneration in osteoarthritis therapy. *Biomedicines*. **2023**;*11*:2244.
137. Makris EA, Gomoll AH, Malizos KN, Hu JC, Athanasiou KA. Repair and tissue engineering techniques for articular cartilage. *Nat Rev Rheumatol*. **2014**;*11*:21.
138. de Ruijter M, Hrynevich A, Haigh JN, Hochleitner G, Castilho M, Groll J, Malda J, Dalton PD. Out-of-plane 3D-printed microfibers improve the shear properties of hydrogel composites. *Small*. **2017**;*14*:1702773.
139. Ghosh Dastidar A, Clarke SA, Larrañeta E, Buchanan F, Manda K. In vitro degradation of 3D-printed poly(l-lactide-co-glycolic acid) scaffolds for tissue engineering applications. *Polymers*. **2023**;*15*:3714.
140. Lu Y, Cui Z, Cheng L, Li J, Yang Z, Zhu H, Wu C. Quantifying the discrepancies in the geometric and mechanical properties of the theoretically designed and additively manufactured scaffolds. *J Mech Behav Biomed*. **2020**;*112*: 104080.
141. Castilho M, Mouser V, Chen M, Malda J, Ito K. Bi-layered micro-fibre reinforced hydrogels for articular cartilage regeneration. *Acta Biomater*. **2019**;*95*:297.
142. Han Y, Jia B, Lian M, Sun B, Wu Q, Sun B, Qiao Z, Dai K. High-precision, gelatin-based, hybrid, bilayer scaffolds using melt electro-writing to repair cartilage injury. *Bioact Mater*. **2021**;*6*:2173.
143. Montoya Y, Cardenas J, Bustamante J, Valencia R. Effect of sequential electrospinning and co-electrospinning on morphological and fluid mechanical wall properties of polycaprolactone and bovine gelatin scaffolds, for potential use in small diameter vascular grafts. *Biomater Res*. **2021**;*25*:38.
144. Zhang F, Cao K, Zaeri A, Zgeib R, Buckley C, Ma Y, Chang RC. Design, fabrication, and characterization of tubular scaffolds by way of a melt electrowriting process. *Addit Manuf*. **2023**;*62*: 103383.
145. Geelhoed WJ, Lalai RA, Sinnige JH, Jongeleen PJ, Storm C, Rotmans JI. Indirect burst pressure measurements for the mechanical assessment of biological vessels. *Tissue Eng Part C Methods*. **2019**;*25*: 472.
146. L'Heureux N, Dusserre N, Konig G, Victor B, Keire P, Wight TN, Chronos NAF, Kyles AE, Gregory CR, Hoyt G, Robbins RC, McAllister TN. Human tissue-engineered blood vessels for adult arterial revascularization. *Nat Med*. **2006**;*12*:361.
147. Kumar VA, Brewster LP, Caves JM, Chaikof EL. Tissue engineering of blood vessels: functional requirements, progress, and future challenges. *Cardiovasc Eng Technol*. **2011**;*2*:137.
148. Chen K, Liu Z, Zhou X, Zheng W, Cao H, Yang Z, Wang Z, Ning C, Li Q, Zhao H. Hierarchy reproduction: multiphasic strategies for tendon/ligament-bone junction repair. *Biomater Res*. **2025**;*29*:0132.
149. Wu Y, Wu B, Vijayavenkataraman S, Wong YS, Fuh JYH. Crimped fiber with controllable patterns fabricated via electrohydrodynamic jet printing. *Mater Des*. **2017**;*131*: 384.
150. Yao K, Lv S, Zhang X, Shen K, Chen Y, Ma Z, He Y. 3D printing of multiscale biomimetic scaffold for tendon regeneration. *Adv Funct Mater*. **2024**;*35*: 2413970.

151. Astuti SD, Utomo IB, Setiawatie EM, Khasanah M, Purnobasuki H, Arifianto D, Alamsyah KA. Combination effect of laser diode for photodynamic therapy with doxycycline on a wistar rat model of periodontitis. *BMC Oral Health*. **2021**;*21*:80.
152. Swanson WB, Yao Y, Mishina Y. Novel approaches for periodontal tissue engineering. *Genesis*. **2022**;*60*: e23499.
153. Almeida ND, Carneiro CA, de Marco AC, Porto VC, França R. 3D bioprinting techniques and bioinks for periodontal tissues regeneration—a literature review. *Biomimetics*. **2024**;*9*:480.
154. Lian M, Han Y, Sun B, Xu L, Wang X, Ni B, Jiang W, Qiao Z, Dai K, Zhang X. A multifunctional electrowritten bi-layered scaffold for guided bone regeneration. *Acta Biomater*. **2020**;*118*: 83.
155. Daghrery A, de Souza Araújo IJ, Castilho M, Malda J, Bottino MC. Unveiling the potential of melt electrowriting in regenerative dental medicine. *Acta Biomater*. **2023**;*156*: 88.
156. Qian Y, Lin H, Yan Z, Shi J, Fan C. Functional nanomaterials in peripheral nerve regeneration: scaffold design, chemical principles and microenvironmental remodeling. *Mater Today*. **2021**;*51*:165.
157. Zhang X, Qu W, Li D, Shi K, Li R, Han Y, Jin E, Ding J, Chen X. Functional polymer-based nerve guide conduits to promote peripheral nerve regeneration. *Adv Mater Interfaces*. **2020**;*7*: 2000225.
158. Liu K, Yan L, Li R, Song Z, Ding J, Liu B, Chen X. 3D printed personalized nerve guide conduits for precision repair of peripheral nerve defects. *Adv Sci*. **2022**;*9*: 2103875.
159. Gao X, Zhang Y, Wu Y, Nguyen TT, Wu J, Guo M, Du C. Inspired by skeletal muscles: study of the physical and electrochemical properties of derived lignocellulose-based carbon fibers. *Materials*. **2022**;*15*: 8068.
160. Vijayavenkataraman S. Nerve guide conduits for peripheral nerve injury repair: a review on design, materials and fabrication methods. *Acta Biomater*. **2020**;*106*:54.
161. Dong X, Liu S, Yang Y, Gao S, Li W, Cao J, Wan Y, Huang Z, Fan G, Chen Q, Wang H, Zhu M, Kong D. Aligned microfiber-induced macrophage polarization to guide schwann-cell-enabled peripheral nerve regeneration. *Biomaterials*. **2021**;*272*: 120767.
162. Zhu R, Sun Z, Li C, Ramakrishna S, Chiu K, He L. Electrical stimulation affects neural stem cell fate and function in vitro. *Exp Neurol*. **2019**;*319*: 112963.
163. Leahy LM, Woods I, Gutierrez-Gonzalez J, Maughan J, O'Connor C, Stasiewicz M, Kaur K, Monaghan MG, Dervan A, O'Brien FJ. Electrostimulation via a 3D-printed, biomimetic, neurotrophic, electroconductive scaffold for the promotion of axonal regrowth after spinal cord injury. *Mater Today*. **2024**;*79*:60.
164. Lou L, Rubfiaro AS, Deng V, He J, Thomas T, Roy M, Dickerson D, Agarwal A. Harnessing 3D printing and electrospinning for multiscale hybrid patches mimicking the native myocardium. *ACS Appl Mater Interfaces*. **2024**;*16*:37596.
165. Zhu G, Zhang T, Chen M, Yao K, Huang X, Zhang B, Li Y, Liu J, Wang Y, Zhao Z. Bone physiological microenvironment and healing mechanism: basis for future bone-tissue engineering scaffolds. *Bioact Mater*. **2021**;*6*:4110.
166. Yang C, Ji J, Lv Y, Li Z, Luo D. Application of piezoelectric material and devices in bone regeneration. *Nanomaterials*. **2022**;*12*:4386.
167. Zhang P, Qi J, Zhang R, Zhao Y, Yan J, Gong Y, Liu X, Zhang B, Wu X, Wu X, Zhang C, Zhao B, Li B. Recent advances in composite hydrogels: synthesis, classification, and application in the treatment of bone defects. *Biomater Sci*. **2024**;*12*: 308.
168. Ye T, Yan J, Kan T, Xie G, Zhang Z, Yin W, Zhao B, Yu Z, Chu L. Articular cartilage degeneration and aberrant osteocyte perilacunar/canalicular remodeling in subchondral bone of patients with developmental dysplasia of the hip. *BMC Musculoskelet Dis*. **2025**;*26*:165.
169. Goins A, Webb AR, Allen JB. Multi-layer approaches to scaffold-based small diameter vessel engineering: a review. *Mat Sci Eng C-Mater*. **2019**;*97*:896.
170. Xie X, Cai J, Li D, Chen Y, Wang C, Hou G, Steinberg T, Rolauffs B, El-Newehy M, El-Hamshary H, Jiang J, Mo X, Zhao J, Wu J. Multiphasic bone-ligament-bone integrated scaffold enhances ligamentization and graft-bone integration after anterior cruciate ligament reconstruction. *Bioact Mater*. **2024**;*31*:178.
171. Xie Z, Zhang P, Zhang Z, Chen C, Wang X. The choice of antimicrobial polymers: Hydrophilic or hydrophobic? *Chin Chem Lett*. **2024**;*35*: 109768.
172. Aghazadeh MR, Delfanian S, Aghakhani P, Homaeigohar S, Alipour A, Shahsavarani H. Recent advances in development of natural cellulosic non-woven scaffolds for tissue engineering. *Polymers*. **2022**;*14*: 1531.